Search for Higgs Bosons of the Minimal Supersymmetric Model at LEP2 with the DELPHI Detector

Esben Lund

Department of Physics

University of Oslo

May 11, 1996

Thesis submitted in partial fulfillment of the requirements to obtain the degree of Cand. Scient. at the University of Oslo

Abstract

This is a study of the exclusion and discovery potential for the h^0 and A^0 Minimal SuperSymmetric Model Higgs bosons, at LEP2, using the DELPHI detector. Three different center-of-mass energies are examined; 175, 192 and 205 GeV. Full simulations of signal and background data are used throughout the analysis.

A search for $h^0A^0 \rightarrow b\bar{b}b\bar{b}$ is prepared, and the expected backgrounds are established. Exclusion and discovery limits are calculated and presented in plots of the total number of observed $b\bar{b}b\bar{b}$ events.

It's shown that the lower mass bounds on h^0 and A^0 will be greatly increased at LEP2.

Acknowledgments

I would like to thank my supervisors Lars Bugge and Alex Read for helping me throughout the work on this thesis. Thanks also goes to Trond Myklebust and Ole Røhne for helping me out with the full simulations and software in general. Thanks to my brother Vidar Lund for comments and ideas. Finally, I want to thank all my fellow students; Bernt Rostad, Sindre Hansen, Jørgen Hansen, Yngve Kvinnsland and Håkon Fløystad, for moral support and helpful comments.

Contents

Chapter 1

Introduction

The Standard Model has been very successful in predicting new particles, and has given us much insight in the forces controlling the interactions between elementary particles.

The Standard Model still has many unknown parameters, mostly due to its missing mass predictions. In fact, the Standard Model prefers zero mass particles. Since some particles obviously have masses, the Higgs mechanism[1] was introduced to allow this. The Higgs mechanism also brought a new boson, the *Higgs boson* (H), into the Standard Model. This boson makes up the universal Higgs field, which some particles couple to, thereby gaining masses, and others don't (like the photon).

Since the Standard Model doesn't give any physical understanding of the mass aspect, and becomes problematic at high energies, many scientists have looked for alternative theories. During the 30 years since its creation some of the most promising new theories have been expansions of the Standard Model into supersymmetric versions (like the Minimal Supersymmetric Model). The Minimal Supersymmetric Model contains heavy superpartners to all the Standard Model particles, and it has a much richer Higgs sector. This Higgs sector contains 5 bosons; h^0, H^0, A^0, $H^\pm$, and 2 free parameters. These are often chosen to be $\tan\beta$ and m_{A^0} for reasons of simplicity. $\tan\beta$ is the ratio of the vacuum expectation values, v_2/v_1, and m_{A^0} is the mass of the pseudoscalar Higgs boson. The Minimal Supersymmetric Model is presented in much more detail in later Chapters.

None of these Higgs bosons have been seen yet, and this analysis was originally intended to look for 2 of them, h^0 and A^0, at LEP2. (LEP2 is the enhanced version of the Large Electron Positron Collider (LEP) at CERN, operating from 96). Since processes involving single Higgs bosons (h^0Z^0) would become serious backgrounds to a search for only h^0A^0, they have been included as signal. This weakens the analysis as a pure Minimal Supersymmetric Model search, since HZ^0 and h^0Z^0 can't be distinguished, but is necessary to get sufficient statistics. After all, finding *any* Higgs boson will be a success.

Doing a Higgs search is a long process, and this is a very short summary of how it's done in this thesis: First, the Minimal Supersymmetric Model is presented. Then, the different Higgs bosons and parameters are described. Special emphasis is put on mass bounds on the h^0 boson. Second, the signal and background production modes and cross sections are presented. Decays and topologies are also studied. Then a small description of the data simulation process is presented, followed by the main analysis. The simulated data are examined and cuts made. Using these cuts, the final backgrounds are calculated, and plots showing the regions of possible discovery or exclusion of the h^0 and A^0 Higgs bosons are shown.

This analysis is one of several[2] future Higgs searches using the DELPHI detector at LEP.

1.1 Previous Higgs Searches

According to the Particle Data Group[3], the Standard Model Higgs boson has been excluded up to a mass of 58.4 GeV with a confidence level of 95%. This limit has been set by LEP and has been pushed up a little (≈65 GeV[4]) during 94–95. LEP has now reached a saturation point and more data won't raise the exclusion limit anymore. Searches for the Standard Model Higgs boson at low energies has been done in many ways[5] to no avail.

In the Minimal Supersymmetric Model case, things get more complicated because the increased number of bosons and free parameters open new possibilities for Higgs boson production, and new ways for the bosons to escape detection.

For some values of $\tan\beta$ and m_{A^0} the cross section for h^0Z^0 is smaller than the Standard Model HZ^0 cross section and the h^0 is therefore not excluded as high as the Standard Model Higgs boson. h^0 has been excluded (with 95% CL) up to a mass of 44 GeV with $\tan\beta$ bigger than 1.

The A^0 is only produced in pair production together with a h^0 at LEP. Since it might be accompanied by a heavier h^0, their pair production can be impossible even for small A^0 masses. This is why the A^0 only has been excluded up to 22 GeV (for $\tan\beta$ between 50 and 1).

1.2 The LEP Accelerator

The Large Electron, Positron (LEP) accelerator at CERN was built during the end of the eighties in a 27 km long circular tunnel, mainly to produce Z^0's. It's the worlds biggest colliding beam e^+e^- accelerator and its beam energy is around 45.5 GeV, giving a CMS energy of 91 Gev, optimized for Z^0 production.

The LEP collider houses four experiments, each with its own detector. The four experiments are: DELPHI, ALEPH, L3 and OPAL.

During the last 5 years these four detectors (experiments) have collected data at LEP. Millions of Z^0's have been produced and many high precision measurements have been made. The confirmation of the 3 fermion families is maybe the most important.

The potential for new discoveries at LEP is exhausted and the next phase (LEP2) of the project has already started. The LEP accelerator will be equipped with new superconducting RF-cavities, doubling the beam energy. The exact number of cavities finally installed is an economic question and is unknown today.

This thesis treats 3 different energies; 175, 192 and 205 GeV, to help deciding which energy to go for. It's shown later in this thesis that the highest possible energy is preferred in the Higgs search, but due to the low e^+,e^- masses synchrotron radiation becomes a major problem around CMS energies of 200 GeV. 192 Gev (phase IV, Table 1.1) is therefore likely to be the final energy. Table 1.1 shows the different phases for the building of LEP2. Two types of cavities are

mentioned, Cu are the old Copper cavities from LEP, and SC are the new superconducting cavities. Maximum beam energies require months of calibration and won't be reached until the final phase is built (probably IV). Phase IV will probably be finished during 1998.

Phase	Cavities (Cu + SC)	L_{max} (cm^{-2} s^{-1})	$E\text{-}beam_{max}$ (GeV)
II	$(120 + 192)$	8.2×10^{31}	90.4
IIIa	$(52 + 224)$	11.6×10^{31}	91.5
IIIb	$(52 + 240)$	10.6×10^{31}	93.4
IV	$(52 + 272)$	10.0×10^{31}	96.5
X1	$(52 + 304)$	9.4×10^{31}	98.7
X2	$(0 + 336)$	9.8×10^{31}	100.5
Y	$(0 + 352)$	9.6×10^{31}	101.7
Z	$(0 + 384)$	5.5×10^{31}	104.2

Table 1.1: Some possible phases of LEP2.

1.3 The DELPHI Detector

Each of the four experiments at LEP are run by several hundred scientists. Scientists and students from the Norwegian universities are participants in the DELPHI experiment[6] (Fig. 1.1). It was built parallel to the LEP accelerator and finished (improvements are still made) during 1989. It's a standard barrel detector with 2 end caps and a superconducting solenoid to generate a 1.2 Tesla magnetic field. The field turns the charged tracks into helices which are vital for determining particle momenta.

Since the collisions at LEP generate a great variety of particles a versatile detector is needed. This is why DELPHI is designed with so many different detector parts.

The design and assembly of a barrel detector is of course not trivial, cracks are bound to exist where the parts are connected. It's desired to not give particles a chance to follow these cracks out of the detector and thereby go undetected. The cracks therefore shouldn't go parallel to the particle tracks. At DELPHI they do, causing much frustration and reduced statistics.

A short description of the most important DELPHI parts:

Vertex Detector (VD) A multi layer silicon detector very close to the interaction point. It gives high precision measurements of charged tracks and their

impact parameters (described later in great detail). The VD has been enhanced several times and is widely used, especially for B-physics and Higgs hunting.

Time Projection Chamber (TPC) Used for measuring the curvature of the tracks inside the magnetic field. The curvature is used for calculating particle momenta and determining charges. The TPC is a drift chamber filled with gas.

Ring Imaging Cherenkov counter (RICH) Used for determining particle velocities. (The velocity, v, together with p and q from the TPC is used for particle identification). It's a very complicated design based on Cherenkov radiation and has had many problems in the past. It has however been running steady during the last 2–3 years. The RICH contains several different gases.

High density Projection Chamber (HPC) Electromagnetic calorimeter, used for determining e^+,e^- and γ energies. The HPC is also filled with gas.

Hadron Calorimeter (HCAL) Used for measuring Hadron (p,n and $\pi^\pm$ mostly) energies, and for separating μ's from hadrons. The HCAL is a combination of iron layers and gas detectors.

Muon Chambers Used for identifying muons, μ. These are drift chambers.

Forward ElectroMagnetic Calorimeter (FEMC) These are the electromagnetic calorimeters located in the end caps of the detector. The FEMC uses lead-glass for the energy measuring.

Forward Chamber A (FCA), and B (FCB) These are tracking and triggering devices located in the end caps. FCA is a streamer chamber and FCB is a drift chamber, both are filled with gas.

STIC,SAT and VSAT Used for measuring Luminosity through Bhabbha scattering. These are electromagnetic calorimeters. The SAT (Small Angle Tagger), has been replaced by the STIC (Small Angle Tile Calorimeter), Fig. 1.1.

From these descriptions it's obvious that DELPHI is a very complex detector. The main problem is to keep the right mixture and temperature in all the different gases of the detector. However, since the VD is the most essential part of a search for Higgs bosons, and DELPHI has a very good VD, it doesn't have any major handicaps for a Higgs search at LEP2.

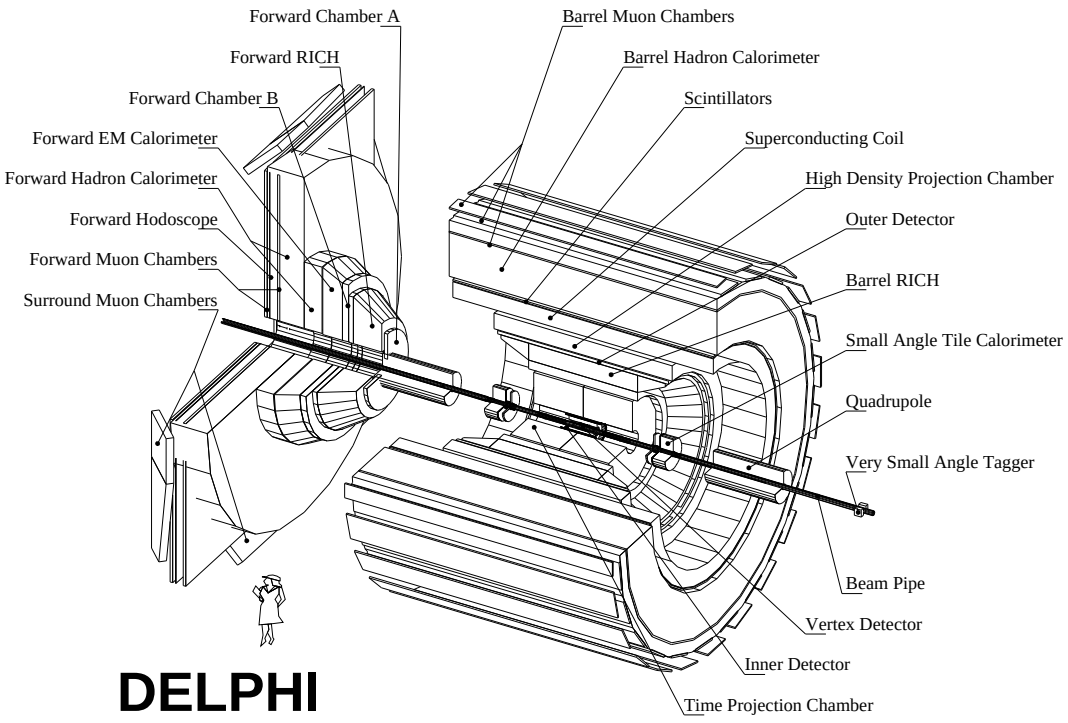

Figure 1.1: The DELPHI detector.

Chapter 2

Higgs Bosons of the Minimal Supersymmetric Model

The Standard Model has been very successful in many ways, but some problems are still left. Many theorists feel that a final theory should incorporate all forces, unifying them into one at a sufficient energy (the GUT scale $\sim 10^{16}$ GeV). Such a theory is called a Grand Unified Theory, or GUT. The Standard Model isn't a GUT, and has other shortcomings too. Why are left-handed fermions in SU(2) doublets and right-handed ones in SU(2) singlets? Why three colours? Why is electric charge quantized? How many generations are there? Why do the Cabibbo-Kobayashi-Maskawa (CKM) angles and the weak mixing angle have the values they do? These questions might never be answered, but their solutions aren't found in the Standard Model.

2.1 Motivation for Going Beyond the Standard Model

Haber and Kane shows in Ref. [7] that if one calculates radiative corrections to the mass of the Higgs boson of the Standard Model, eg. from a fermion loop in the propagator, one has a loop integral of the form:

$$\int d^4P [\frac{\not{P} + \not{K} - m_f}{\not{P} - m_f}]$$

for a Higgs of momentum K. This diverges quadratically for large P, independently of K, so it gives a correction $\delta m^2 \sim \lambda^2$ where λ is the scale beyond which the low energy theory no longer applies. For some Higgs mass of the order of a few TeV, the Higgs self-coupling gets too strong, and we shouldn't be observing the apparently successful perturbation theory at low energies. Since corrections larger than this mass scale are equally unphysical, we expect the new physics to give an effective cutoff scale below a few TeV. In fact, the Higgs vacuum expectation value, which determines m_W and, in principal, the fermion masses, is about 250 GeV, and it's this number that needs a fundamental explanation. Which mechanism can prevent the Higgs from becoming superheavy? (which it can't be in the Standard Model).

Several approaches have been used to produce this low Higgs mass, Technicolour and supersymmetry being the best studied. Technicolour is however very hard to work with and predicts low mass technipions (below 25 GeV) which haven't been seen. Supersymmetry goes to a higher symmetry to eliminate the quadratic divergence, and does so very successfully.

It's useful to restate the above arguments in a more theoretical manner for clarity. Let μ_2 be the scale at which SU(2)×U(1) (electroweak) breaking takes place. We assume that the Standard Model is the low energy approximation of some more fundamental theory which becomes relevant at a scale μ_1 (The GUT scale). We calculate the mass of the Standard Model Higgs boson using

the fundamental theory. This produces the scale dependent mass parameter evaluated at the fundamental scale μ_1. The relevant quantity at low energies is the running mass evaluated at the electroweak scale, μ_2. These two quantities are related by an equation which has the schematic form[8]:

$$m_H^2(\mu_2) = m_H^2(\mu_1) + Cg^2 \int_{\mu_2^2}^{\mu_1^2} dk^2 + Rg^2 + O(g^4), \tag{2.1}$$

where g is a coupling constant, C is dimensionless and R grows almost logarithmically with μ_1 as $\mu_1 \to \infty$. The term proportional to C diverges quadratically when $\mu_1 \to \infty$. This equation illustrates the theoretical problems described above. First, in order that $m_H^2(\mu_2) \ll \mu_1^2$, one has to fine-tune the parameter $m_H^2(\mu_1)$ extremely accurately to cancel the second term in Eq. (2.1) which is of order μ_1^2. This is called the fine-tuning problem. It has also been referred to as the naturalness problem; clearly the "natural" value for $m_H^2(\mu_2)$ is a number of order μ_1^2. A related problem is the hierarchy problem; Why is $\mu_2 \ll \mu_1$?

These problems are solved in supersymmetry by introducing supersymmetric partners to all the known particles. These are in principal similar in mass and quantum numbers, except for their spin, which is shifted by one-half. When these partners are included in the calculation all quadratic divergences disappear ($C \equiv 0$ in Eq. (2.1)). This happens because certain Feynman diagrams cancel when introducing superpartner loops accompanying the loops of the normal particles. The extra minus sign that goes with any fermion loop, plus the supersymmetric relations between masses and couplings, removes the quadratic Higgs mass divergence, and the need for an unnatural fine-tuning of parameters.

Since such superpartners haven't been seen yet, they must have higher masses than their normal partners, ie. the symmetry is broken. $C \neq 0$, but might still be small enough to work things out. As long as effects of supersymmetry become relevant by a scale of $\mu_1 \sim$1 TeV (ie. new supersymmetric particles have masses below or equal to μ_1), naturalness is preserved. Our problems aren't solved if this scale is above 1 TeV. This scale is called; The supersymmetry breaking scale, M_S, and is set to 1 TeV throughout this thesis.

To sum it up: The fine-tuning problem indicates physics beyond the Standard Model, and supersymmetry is a good solution. Supersymmetry implies a spectrum of new particles with masses below, or equal to, 1 TeV. The lightest of which should be around m_W.

Another interesting aspect of supersymmetry is the possibility to incorporate gravity. Supersymmetric transformations are intimately tied up with space-time ones, giving hopes of incorporating gravity into a final Supersymmetric Grand Unified Theory.

2.2 Supersymmetric Models

Before introducing the theoretical aspects of the Minimal Supersymmetric Model, some things should be mentioned about supersymmetric models in general.

First, a supersymmetric model needs two Higgs doublets (The Standard Model has one) to give masses to both up-type and down-type quarks and leptons. In addition, a multiplicatively conserved quantum number called R-parity is introduced. All ordinary particles are assigned a R-parity of +1, and all their supersymmetric partners are given a R-parity of -1. Formally, one can define the R-parity of any particle of spin j, baryon number B and lepton number L to be $R = (-1)^{2j+3B+L}$. This has important consequences; Supersymmetric particles must be produced in pairs, and there must exist a "ground-state" supersymmetric particle. This lightest supersymmetric particle must be stable since R-parity isn't conserved if it decays into only ordinary particles. Such a particle is a good candidate to the missing dark matter in the universe.

R-parity doesn't put any constraints on this analysis since the h^0 and A^0 aren't supersymmetric particles. Their supersymmetric partners are called Higgsinos.

2.2.1 The General Two-Doublet Model

A more thorough look at the theory can be found in Refs. [5, 9].

First, a general look at the two-doublet Higgs model is presented. This produces the 5 Higgs bosons and their quantum numbers. Then the model is reduced to the Minimal Supersymmetric Model, which limits the number of free parameters and constrains the possible Higgs boson masses.

The doublets of the general two complex doublets model look like this:

$$\phi_1 = \begin{pmatrix} \phi_1^+ \\ \phi_1^0 \end{pmatrix}, \quad \phi_2 = \begin{pmatrix} \phi_2^+ \\ \phi_2^0 \end{pmatrix} \tag{2.2}$$

Using these doublets and the fact that the most general gauge invariant Higgs potential must respect the discrete symmetry $\phi_1 \leftrightarrow -\phi_1$ in order to avoid Flavour-Changing Neutral Currents at tree level, the Higgs potential takes the form:

$$\begin{aligned} V(\phi_1, \phi_2) = \; & \lambda_1(\phi_1^\dagger\phi_1 - v_1^2)^2 + \lambda_2(\phi_2^\dagger\phi_2 - v_2^2)^2 \\ & +\lambda_3[(\phi_1^\dagger\phi_1 - v_1^2) + (\phi_2^\dagger\phi_2 - v_2^2)]^2 \\ & +\lambda_4[(\phi_1^\dagger\phi_1)(\phi_2^\dagger\phi_2) - (\phi_1^\dagger\phi_2)(\phi_2^\dagger\phi_1)] \\ & +\lambda_5[Re(\phi_1^\dagger\phi_2) - v_1 v_2 \cos\xi]^2 \\ & +\lambda_6[Im(\phi_1^\dagger\phi_2) - v_1 v_2 \sin\xi]^2 \end{aligned} \tag{2.3}$$

This potential has eight Higgs fields, or degrees of freedom; $\lambda_i (i = 1, ..., 6)$ and the vacuum expectation values v_1 and v_2.

The Vacuum Expectation Values;

$$v_1 = <\phi_1> = \begin{pmatrix} 0 \\ v_1 \end{pmatrix}, \quad v_2 = <\phi_2> = \begin{pmatrix} 0 \\ v_2 e^{i\xi} \end{pmatrix}$$

minimize the potential for arbitrary positive parameters $\lambda_i (i = 1, ..., 6)$ and arbitrary phase ξ. This potential with spontaneously broken symmetry is analogous to the Standard Model potential.

For $\sin \xi \neq 0$, the CP symmetry of the Lagrangian is broken due to the phase ξ. This leads to large CP violation, in contradiction to measurements, thus, ξ is set to zero. (In the Standard Model, CP violation can be incorporated by introducing a CP violating phase in the CKM matrix).

The Higgs spectrum is obtained by expanding the Higgs fields around their minima. Three Goldstone bosons are identified by their derivative couplings to the gauge fields. Performing the expansion of the gauge invariant terms in the Lagrangian $\mathcal{L} = |D_\mu \phi_1|^2 + |D_\mu \phi_2|^2 + ...$ with the covariant derivative $D_\mu = (\partial_\mu - \frac{i}{2} g \tau \cdot W_\mu - \frac{i}{2} g' \tau X_\mu)$, the gauge boson masses and an orthogonal basis of the neutral gauge boson mass eigenstates are obtained. The resulting gauge boson masses are given by:

$$m_W^2 = (v_1^2 + v_2^2)\frac{g^2}{2}, \quad m_\gamma = 0, \quad m_Z^2 = (v_1^2 + v_2^2)\frac{g^2}{2\cos^2\theta_W}, \tag{2.4}$$

where $g = \frac{e}{\sin\theta_W}$. Thus, the quadratically summed vacuum expectation values(VEV) must be equal to the VEV of the Standard Model. The ratio of the VEV defines a key parameter;

$$\tan\beta \equiv \frac{v_2}{v_1}$$

H^0 and h^0 mix through the following mass-squared matrix:

$$M = \begin{pmatrix} 4v_1^2(\lambda_1 + \lambda_3) + v_2^2\lambda_5 & (4\lambda_3 + \lambda_5)v_1 v_2 \\ (4\lambda_3 + \lambda_5)v_1 v_2 & 4v_2^2(\lambda_2 + \lambda_3) + v_1^2\lambda_5 \end{pmatrix} \tag{2.5}$$

Diagonalization introduces a second key parameter; The neutral mixing angle, α.

Physical Higgs boson masses for 2 charged Higgs bosons, $H^\pm$, and 3 neutral Higgs bosons, h^0, H^0 and A^0 are obtained:

$$\begin{aligned} &m_{H^\pm}^2 = \lambda_4(v_1^2 + v_2^2), \quad m_{A^0}^2 = \lambda_6(v_1^2 + v_2^2), \\ &m_{H^0,h^0}^2 = \tfrac{1}{2}[M_{11} + M_{22} \pm \sqrt{(M_{11} - M_{22})^2 + 4M_{12}^2}] \end{aligned} \tag{2.6}$$

The convention $m_{H^0} > m_{h^0}$ is adopted.

Thus, the mass spectrum, which is derived from the gauge invariant CP-conserving Higgs potential with spontaneously broken symmetry, consists of five physical Higgs bosons. Of the eight initial Higgs fields (or degrees of freedom) three are Goldstone bosons which are absorbed ("eaten") by $W^\pm$ and Z^0, as in the Standard Model. This leaves 5 Higgs fields(bosons) in the two-doublet model and only 1 Higgs field(boson) in the one-doublet Standard Model.

Instead of the one free parameter of the Standard Model Higgs sector, the general two-doublet model has six free parameters; Four Higgs masses, $m_{H^\pm}$, m_{A^0}, m_{H^0}, m_{h^0}, the ratio of the vacuum expectation values, $\tan\beta$, and the neutral mixing angle, α. These six free parameters in the Higgs sector leaves the general two-doublet model with very little predictive power.

2.2.2 Allowed Higgs Boson Production Modes of the General Two-Doublet Model at LEP2

The charge conjugation, C, parity, P, and total angular momentum, J, quantum numbers of the Higgs bosons allows us to identify the possible Higgs production mechanisms at LEP2. The J^{PC} quantum numbers are 1^{--} for the photon, 1^{--} for the Z^0, and 1^- for the $W^{\pm}$. C isn't defined for charged particles ($W^{\pm}$). These quantum numbers must be conserved during the Higgs production process.

Applying the parity and charge conjugation operators to the Higgs fields, the following quantum numbers are assigned, J^{PC}:

- A^0, 0^{+-}. Pseudoscalar, but transforms as a scalar.
- H^0 and h^0, 0^{++}. Scalar.
- $H^{\pm}$, $0^+(J^P)$. Scalar, again C isn't defined for charged particles.

The CP-odd nature of A^0 forbids its bremsstrahlung emission off the Z^0 or the $W^{\pm}$. Furthermore, the interactions $Z^0 \rightarrow h^0h^0$ and $Z^0 \rightarrow A^0A^0$ are forbidden by Bose statistics (the Z wave function is antisymmetric, while Bose statistics requires a symmetric wave function for the AA state). The only remaining interactions for the Higgs production, at LEP2, are:

- The Bjorken process: $Z^* \rightarrow H^0Z^0, \quad h^0Z^0$.
- Neutral pair production: $Z^* \rightarrow H^0A^0, \quad h^0A^0$.
- Charged pair production: $Z^* \rightarrow H^+H^-$.

2.2.3 The Minimal Supersymmetric Model

As mentioned before, the general two-doublet model has too little predictive power to be of much interest to experimentalists, so further constrains are applied. The Minimal Supersymmetric Model is born.

Two Higgs fields, analogous to the ones in Eq. (2.2), are introduced:

$$H_1 = \begin{pmatrix} \phi_1^0 \\ \phi_1^- \end{pmatrix}, \quad H_2 = \begin{pmatrix} \phi_2^+ \\ \phi_2^0 \end{pmatrix}$$

The supersymmetry breaking terms in the Lagrangian are constrained in order not to destroy the main motivation for supersymmetry, the cancellation of the quadratic cut-off contributions to the Higgs boson mass. The required cancellation relates the gauge boson couplings to the Higgs couplings and results in the experimentally relevant mass relations between the five Higgs bosons.

The scalar potential, V, which describes the bosonic Higgs sector is derived from the superpotential, W (for more info on the superpotential see Refs. [5]

and [9]). After adding soft supersymmetry breaking mass terms and rearranging the terms to recover the form of the potential of the general two-doublet model ,Eq. (2.3), the bosonic Higgs potential in the Minimal Supersymmetric Model is given by:

$$\begin{aligned} V = \quad & (m_1^2 + |\mu|^2) H_1^{i*} H_1^i + (m_2^2 + |\mu|^2) H_2^{i*} H_2^i \\ & - m_{12}^2 (\epsilon_{ij} H_1^i H_2^j + h.c.) \\ & + \tfrac{1}{8}(g^2 + g'^2)[H_1^{i*} H_1^i + H_2^{j*} H_2^j]^2 + \tfrac{1}{2} g^2 \, |H_1^{i*} H_2^i|^2 \end{aligned} \tag{2.7}$$

Hence, the same five physical Higgs fields, which are identified in the general two-doublet model, are expanded around their VEV. The comparison of the above supersymmetric Higgs potential with the potential of the general two-doublet model leads to constraints on the six λ degrees of freedom of the general model:

$$\begin{aligned} & \lambda_1 = \lambda_2 \\ & \lambda_3 = \tfrac{1}{8}(g^2 + g'^2) - \lambda_1 \\ & \lambda_4 = 2\lambda_1 - \tfrac{1}{2} g'^2 \\ & \lambda_5 = \lambda_6 = 2\lambda_1 - \tfrac{1}{2}(g^2 + g'^2) \end{aligned} \tag{2.8}$$

The last relation assures CP conservation, since the complex phase ξ of the general two-doublet model can be absorbed by a field redefinition.

Relations for the m_i parameters are also found by comparison with the two-doublet potential:

$$\begin{aligned} m_1^2 &= -|\mu|^2 + 2\lambda_1 v_2^2 - \tfrac{1}{2} m_Z^2 \\ m_2^2 &= -|\mu|^2 + 2\lambda_1 v_1^2 - \tfrac{1}{2} m_Z^2 \\ m_{12}^2 &= -\tfrac{1}{2} v_1 v_2 (g^2 + g'^2 - 4\lambda_1) \end{aligned}$$

By combining equations (2.8), (2.6), (2.5) and (2.4), some very important mass relations are derived:

$$\begin{aligned} & m_{H^\pm}^2 = m_{A^0}^2 + m_W^2 \\ & m_{H^0,h^0}^2 = \tfrac{1}{2}[m_{A^0}^2 + m_Z^2 \pm \sqrt{(m_{A^0}^2 + m_Z^2)^2 - 4 m_Z^2 m_{A^0}^2 \cos^2 2\beta}] \end{aligned} \tag{2.9}$$

In addition, the neutral mixing angle, α, can be computed using:

$$\cos 2\alpha = -\cos 2\beta \left(\frac{m_{A^0}^2 - m_Z^2}{m_{H^0}^2 - m_{h^0}^2} \right), \quad \sin 2\alpha = -\sin 2\beta \left(\frac{m_{H^0}^2 + m_{h^0}^2}{m_{H^0}^2 - m_{h^0}^2} \right)$$

By going from a general two-doublet supersymmetric model to the Minimal Supersymmetric Model the number of free parameters is reduced from six (four masses, $\tan\beta$ and α) to two. The parameters m_{A^0} and $\tan\beta$ have been considered the most convenient choice by the theorists, and have therefore been adopted in this thesis.

The m_{A^0}-$\tan\beta$ region analyzed in this thesis is:

- $m_{A^0} \in \{0, 400 \text{ GeV}\}$

- $\tan\beta \in \{1, 60\}$

The mass relations presented in Eq. (2.9) have some very important implications for Higgs searches at LEP2 and LHC;

$$m_{H^\pm} \geq m_W, \;\; m_{H^0} \geq m_Z, \;\; m_{A^0} \geq m_{h^0}$$
$$m_{h^0} \leq m_Z \; |\cos 2\beta| \leq m_Z$$

If m_{h^0} is indeed below m_Z chances of discovery at LEP2 are very good.

The upper bound on m_{h^0} is however raised by radiative corrections. Since the supersymmetry isn't perfect (because the particles and their superpartners are degenerate in mass), the particle and superpartner loop diagrams (of the Higgs boson mass corrections) don't cancel completely. These corrections have been calculated to the second order, and are especially strong for h^0 (m_{h^0} is raised). They stem mainly from top quark loop diagrams, and grow as the fourth power of the top mass, and the logarithm of the ratio of the supersymmetric top mass to the top mass[10].

In addition, these radiative corrections include several obscure parameters without any clear physical interpretation. Such as, the trilinear soft breaking term A, and the supersymmetric Higgs mass parameter μ. These terms determine the mixing between the left and right handed supersymmetric tops, which again affects the upper limit on the h^0 mass. This mixing is proportional to $(A - \frac{\mu}{\tan\beta})$, and influences the h^0 mass and the neutral mixing angle, α, significantly. Three A, μ combinations have therefore been examined for each E_{cms}. These combinations are presented in each exclusion and discovery plot in Chapter 7.

The supersymmetry breaking scale, M_S, also enters the corrections and is taken to the maximum acceptable; 1 TeV, in all plots. The masses of the left- and right-handed top superpartners are also maximized, ie. set to M_S. This is done to study the effects of large radiative corrections to the h^0 mass. The choices of A and μ are motivated in the same way. (The top mass has been set to 175 GeV throughout this analysis). In the worst case scenario the upper limit for m_{h^0} is raised from m_Z (on tree level) to ~ 130 GeV.

The three A, μ combinations used in this thesis produce these upper limits for m_{h^0} (within the $\tan\beta \in \{1, 60\}, m_{A^0} \in \{0, 400 \text{ GeV}\}$ region):

1. $A = \mu = 0$; $m_{h^0} < 115$ GeV. No left-right supersymmetric top mixing.
2. $A = M_S$, $\mu = -M_S$; $m_{h^0} < 120$ GeV. Large mixing in the low-$\tan\beta$ region.
3. $A = \sqrt{6}M_S$, $\mu = 0$; $m_{h^0} < 130$ GeV. Large mixing in the high-$\tan\beta$ region.

A three dimensional plot of m_{h^0} with $A = \mu = 0$ is shown in Fig. 2.1. The plot looks quite similar for the other A and μ combinations, with the plateau at a higher level. (More on A and μ can be found in Refs. [5, 10, 11]).

The chosen m_{A^0}-tan β region isn't arbitrary. The upper limit on m_{A^0} is based on the fact that very little changes in the m_{h^0} plot (Fig. 2.1) and in the cross section plot(Fig. 3.3) beyond this limit. The upper limit on tan β is motivated by the need to keep the running Higgs fermion Yukawa couplings finite at all energy scales [10]. Contrary to the m_{A^0} case, going beyond the upper tan β limit alters the m_{h^0} plot significantly. A "ridge" rises along the left edge (m_{A^0} =100–150 GeV) of the plateau when going to high tan β. The h^0 mass increases by 15–30 GeV when going from tan $\beta = 60$ to tan $\beta = 400$ along this ridge. The h^0 mass is constant at the right edge ($m_{A^0} = 400$ GeV) of the plateau. (The ridge is smallest and at lowest m_{A^0} in the $A = \mu = 0$ case). This ridge isn't seen in the cross section plot, because the h^0A^0 cross section is zero in the m_{A^0} region of the ridge at LEP2 energies.

The lower limit on m_{A^0} is obvious, while the tan β limit of 1 needs more explanation. In supergravity model building, a large t quark Yukawa coupling is used to trigger SU(2)×U(1) breaking in the low-energy theory[12]. This leads to the result that tan $\beta > 1$. It has also been noted[13] that with a large top mass, certain types of models, when evolved from a large mass scale to the weak scale, yield consistent solutions with fairly large tan β values. In general, tan $\beta = 1$ has been accepted by most theorists as the lower limit.

2.3 Grand Unified Theories

As mentioned in the beginning of this Chapter, most theorists believe that the final theory should be a Grand Unified Theory. One of the first requirements of a Grand Unified Theory is the convergence of the three gauge couplings, $\alpha_i (i = 1, 2, 3)$ at some scale M_{GUT}. Using the LEP measurements of the Standard Model gauge couplings, Eq. (2.10), and then scaling up towards the Planck Scale (10^{19} GeV) shows a convergence of the couplings around $M_{GUT} \sim 10^{16}$ GeV in the Minimal Supersymmetric Model case, Fig. 2.2. No convergence is seen in the Standard Model case. This difference stems from the different particle content of the models.

These plots, Fig. 2.2 do however assume that no new particles appear between the supersymmetry breaking scale of one TeV and the GUT scale of around 10^{16} GeV. Such new particles will change the slope of the curves at their relevant scale, and can easily destroy the nice Minimal Supersymmetric Model plot. In addition another larger symmetry is needed to prevent the minimal supersymmetric gauge couplings from diverging above the GUT scale. (see Ref. [4] for more on this).

The Standard Model gauge couplings and $\sin\theta_W$, have these values at the

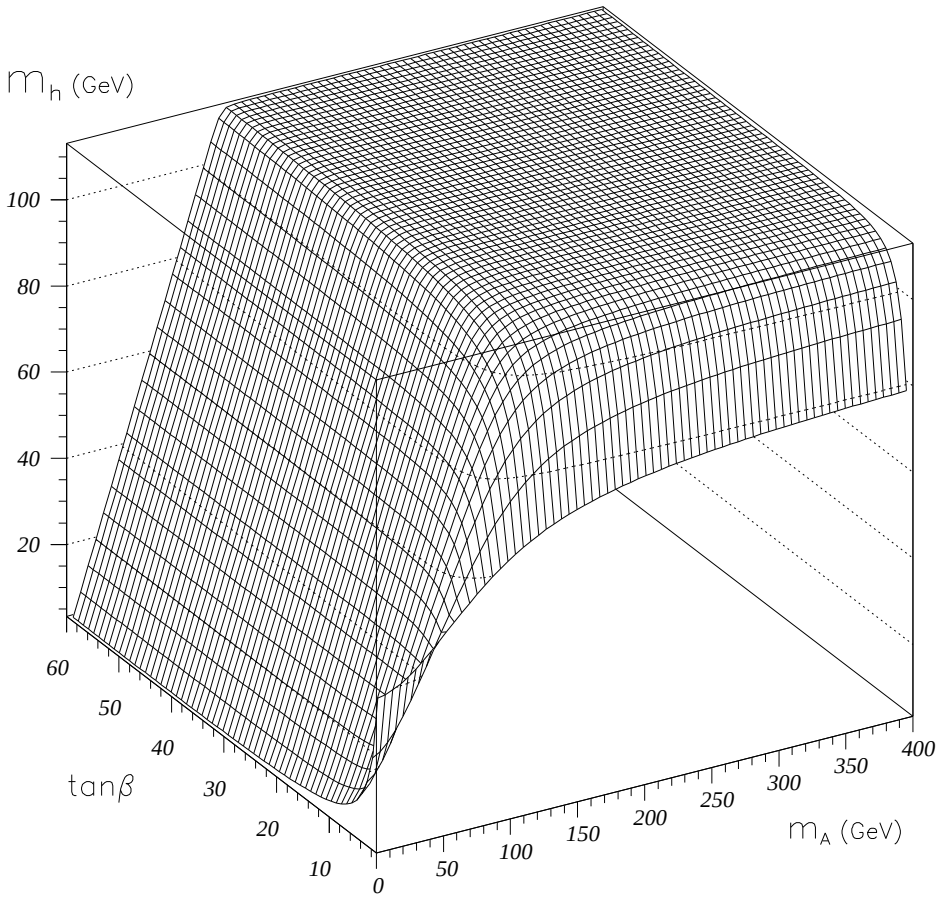

Figure 2.1: The h^0 mass in the m_{A^0}-tan β plane with $A = \mu = 0$.

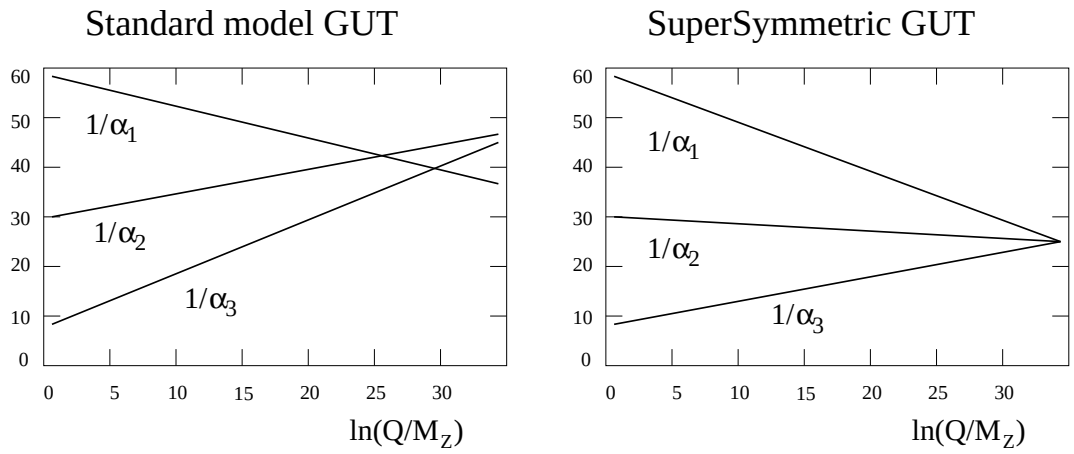

Figure 2.2: Lowest order comparison of the gauge coupling convergence of the Standard Model and Minimal Supersymmetric Model.

weak scale (M_Z):

$$\begin{aligned}
\alpha_1(M_Z) &= \tfrac{5}{3\cos^2\theta_W}(\tfrac{1}{127.9\pm0.1}) \\
\alpha_2(M_Z) &= \tfrac{1}{\sin^2\theta_W}(\tfrac{1}{127.9\pm0.1}) \\
\alpha_3(M_Z) &= 0.118 \pm 0.006 \\
\sin^2\theta_W(M_Z) &= 0.23186 \pm 0.00034
\end{aligned} \tag{2.10}$$

In addition to looking at the converging gauge couplings (bottom-up approach) it's possible to construct Grand Unified Theories and examine their implications on the electroweak scale. This is called a top-down approach.

At the GUT scale the weak mixing angle, $\sin^2\theta_W(M_{GUT})$, is exactly 3/8. The predictions for $\sin^2\theta_W$ at the electroweak scale (calculated to the lowest order) are; For the Standard Model GUT:

$$\sin^2\theta_W(M_Z) = \frac{1}{6} + \frac{5}{9}\frac{\alpha}{\alpha_3} \approx 0.203$$

And for the Supersymmetric GUT:

$$\sin^2\theta_W(M_Z) = \frac{1}{5} + \frac{7}{15}\frac{\alpha}{\alpha_3} \approx 0.230$$

The fine-structure constant, α, is around 1/128 at the electroweak scale. The measured value of $\sin^2\theta_W(M_Z)$, Eq. (2.10), is 0.23186 ± 0.00034. Again, supersymmetry behaves better than the Standard Model.

In this Chapter several problems indicating physics beyond the Standard Model have been presented, and supersymmetry has some of the best solutions to these problems. This explains the increased interest in supersymmetry lately.

Chapter 3

h^0 and A^0 Production Modes and Decays at LEP2

Since the Minimal Supersymmetric Model has five Higgs bosons as opposed to the single H in the Standard Model, the number of processes containing Higgs bosons is greatly increased. Theoretically the H^0, H^+ and H^- are too heavy for LEP2, so this analysis concentrates on h^0 and A^0. While there is only one main production mode in the Standard Model, the Bjorken process[14] (Fig. 3.1), there are two in the Minimal Supersymmetric Model; The Bjorken process and pair production (Fig. 3.2). The rest of the production processes[5] are neglected here due to their small cross sections.

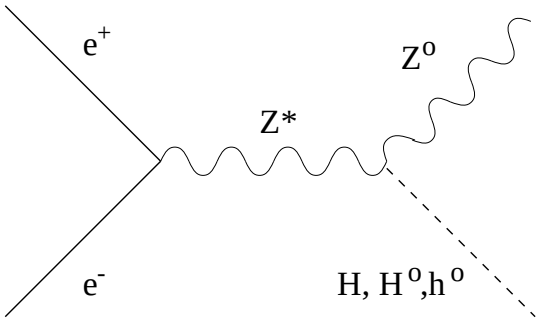

Figure 3.1: The Bjorken process.

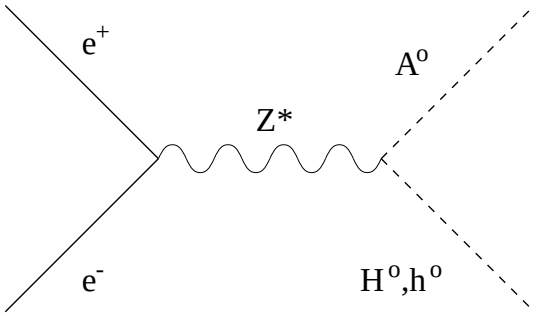

Figure 3.2: Higgs boson pair production.

3.1 Signal Cross Sections

The tree level cross section for $e^+e^- \rightarrow h^0Z^0$ is:

$$\sigma_{h^0Z^0}(\text{tree level}) = \sin^2(\beta - \alpha)\sigma_{H_{SM}Z^0}, \tag{3.1}$$

where $\sigma_{H_{SM}Z^0}$ is the Standard Model cross section[5].

The tree level cross section[5] for $e^+e^- \rightarrow h^0A^0$ is:

$$\sigma_{h^0A^0}(\text{tree level}) = \frac{1}{2}\cos^2(\beta-\alpha)B^3\sigma_{Z^0\rightarrow\nu\bar{\nu}}, \tag{3.2}$$

where B is a phase space factor.

The full tree level expression[15] for $\sigma_{h^0A^0}$ is:

$$\sigma_{h^0A^0}(\text{tree}) = \frac{g^4\cos^2(\beta-\alpha)(8\sin^4\theta_W - 4\sin^2\theta_W + 1)}{1536\cos^4\theta_W}\frac{[(s+m_h^2-m_A^2)^2-4sm_h^2]^{3/2}}{s^2[(s-m_Z^2)^2+?_Z^2m_Z^2]}$$

These cross sections don't include Initial State Radiation (ISR) which reduces them considerably for high Higgs masses. Good approximations of the cross sections, with ISR included, are given by these expressions[16]:

$$\sigma_{h^0Z^0} = 0.938[1-\frac{(m_{h^0}+m_{Z^0})^2}{s}]^{0.115}\sigma_{h^0Z^0}(\text{tree level}) \tag{3.3}$$

$$\sigma_{h^0A^0} = (1-\frac{4m_h^2}{s})^{0.115}\sigma_{h^0A^0}(\text{tree level}) \tag{3.4}$$

Both cross sections, $\sigma_{h^0A^0}$ and $\sigma_{h^0Z^0}$[17], with ISR[16] and second order corrections[11] to m_{h^0} and α, are found in Fig. 3.3. ($\sigma_{h^0A^0}$ to the left and $\sigma_{h^0Z^0}$ at the bottom of the plot).

3.2 h^0 and A^0 Decays

Knowledge of particle decays are of course vital to identify unstable particles. Since h^0 and A^0 are thought to "give" particles masses by coupling to them, particles with big masses have big Higgs couplings. These couplings are proportional to the squared masses of the decay particles, making $b\bar{b}$ the major decay mode, since the top quark is too heavy for LEP2. The supersymmetric particles aren't included as decay modes since none has been observed. The photino ($\tilde{\gamma}$), probably the lightest supersymmetric particle, has been excluded up to 15 GeV (CL=90%)[3]. Supersymmetric decay modes would also make this analysis too complicated.

The decay widths for χ (=h^0, A^0) are[5]:

$$?(\chi\rightarrow q\bar{q}) = 3\kappa m_q^2 m_\chi \xi[1-\frac{4m_q^2}{m_\chi^2}]^p \tag{3.5}$$

$$\xi = \begin{cases} \frac{\cos^2\alpha}{\sin^2\beta} & \chi = h^0, \quad \text{q=up-type quark} \\ \frac{\sin^2\alpha}{\cos^2\beta} & \chi = h^0, \quad \text{q=down-type quark} \\ \cot^2\beta & \chi = A^0, \quad \text{q=up-type quark} \\ \tan^2\beta & \chi = A^0, \quad \text{q=down-type quark} \end{cases} \quad p = \begin{cases} 3/2 & \chi = h^0 \\ 1/2 & \chi = A^0 \end{cases} \quad \kappa = \frac{g^2}{32\pi m_W^2}$$

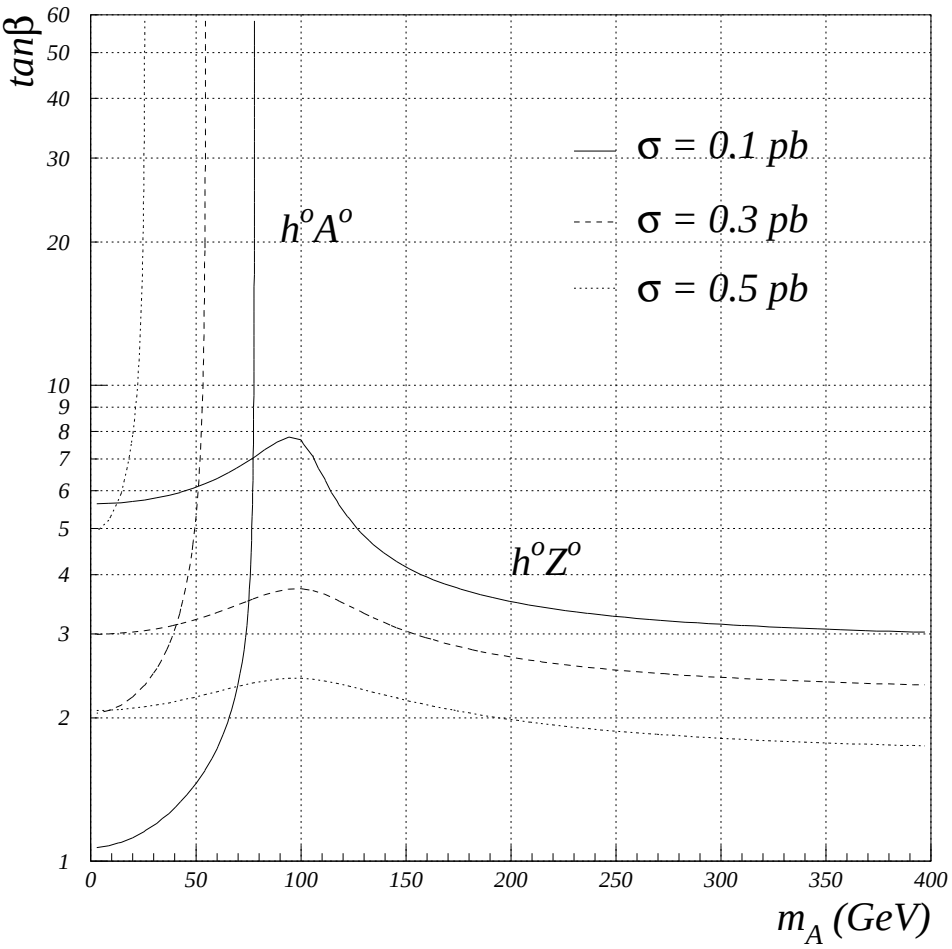

Figure 3.3: The h^0A^0 and h^0Z^0 cross sections in the m_{A^0}-tan β plane for E_{cms} = 192 GeV. $M_S = 1$ TeV, and $A = \mu = 0$.

Equation (3.5) also applies to lepton final states if the colour factor of 3 is removed. Neutrinos couple as up-type quarks and e,μ and τ couple as down-type quarks. The neutrinos have very small couplings, if any at all, due to their small (maybe zero) masses. The τ is the only lepton with considerable Higgs couplings.

3.3 Signal Topology

The most important decay modes of h^0 and A^0 at LEP2 are $\tau\bar{\tau}$ and $b\bar{b}$, because $?_{\tau\bar{\tau}} \approx 6\%$ and $?_{b\bar{b}} \approx 93\%$ for both h^0 and A^0 in most of the m_{A^0}-tan β region. The only exception is when $\tan\beta \approx 1$, then $?_{c\bar{c}}$ becomes comparable to $?_{\tau\bar{\tau}}$.

Since tagging τ's at DELPHI is much harder than tagging b's, and as much as 86% of the h^0A^0 pair productions end up as $b\bar{b}b\bar{b}$, this analysis is specialized in recognizing $b\bar{b}b\bar{b}$ events.

Fig. 3.4[18] is made directly from a simulated $HZ^0 \rightarrow b\bar{b}b\bar{b}$ event (using Pythia[19] and Jetset[20]) and therefore contains all the tracks of the event. The momentum of each particle is given by their length (1 mm=1 GeV). Fig. 3.5 shows a generated $h^0A^0 \rightarrow b\bar{b}b\bar{b}$ event. The three layers of the DELPHI Vertex Detector are shown, with the particle tracks in the x-y plane (z=beam axis). There's 5 cm between the vertex and the inner layer. This event went through the whole simulation procedure (Fig. 5.1), and shows the tracks as seen by DELPHI. The dashed tracks are neutral and are therefore not affected by the magnetic field, whereas the solid lines are charged and thereby bent by the B-field.

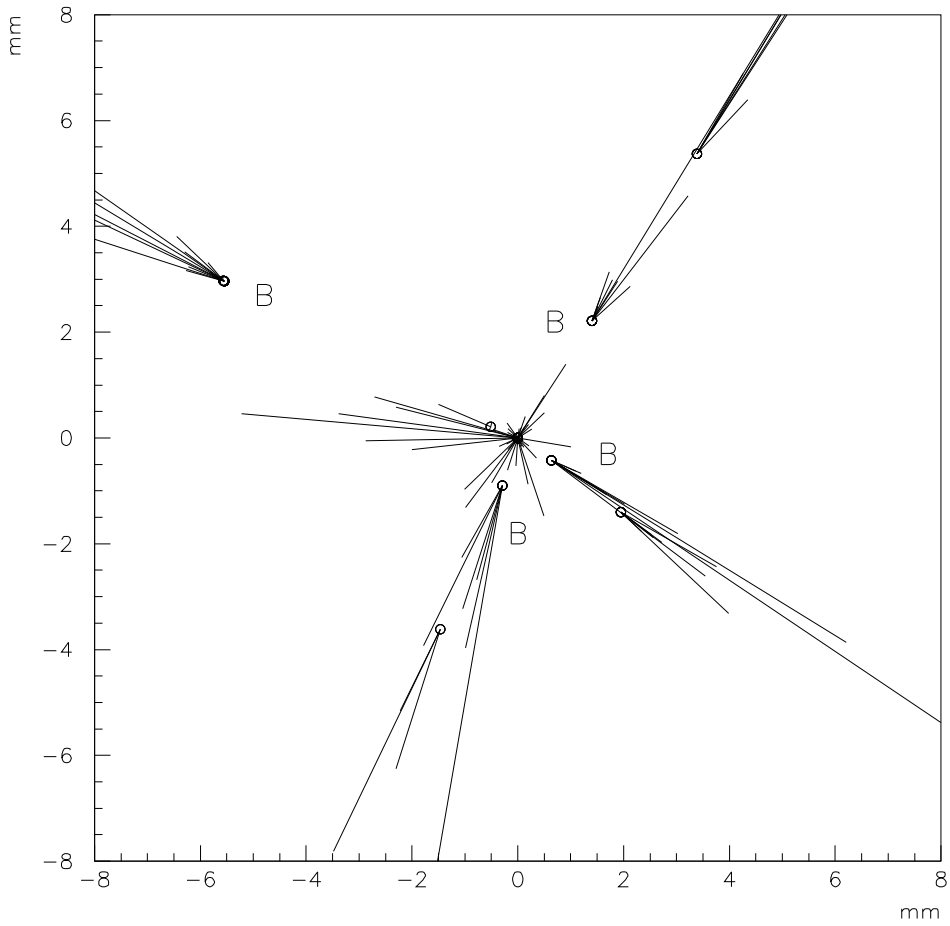

Figure 3.4: The secondary vertices of a generated $HZ^0 \to b\bar{b}b\bar{b}$ event. $E_{cms} = 192$ GeV and $m_H = 80$ GeV. The momenta of the tracks are one GeV per mm.

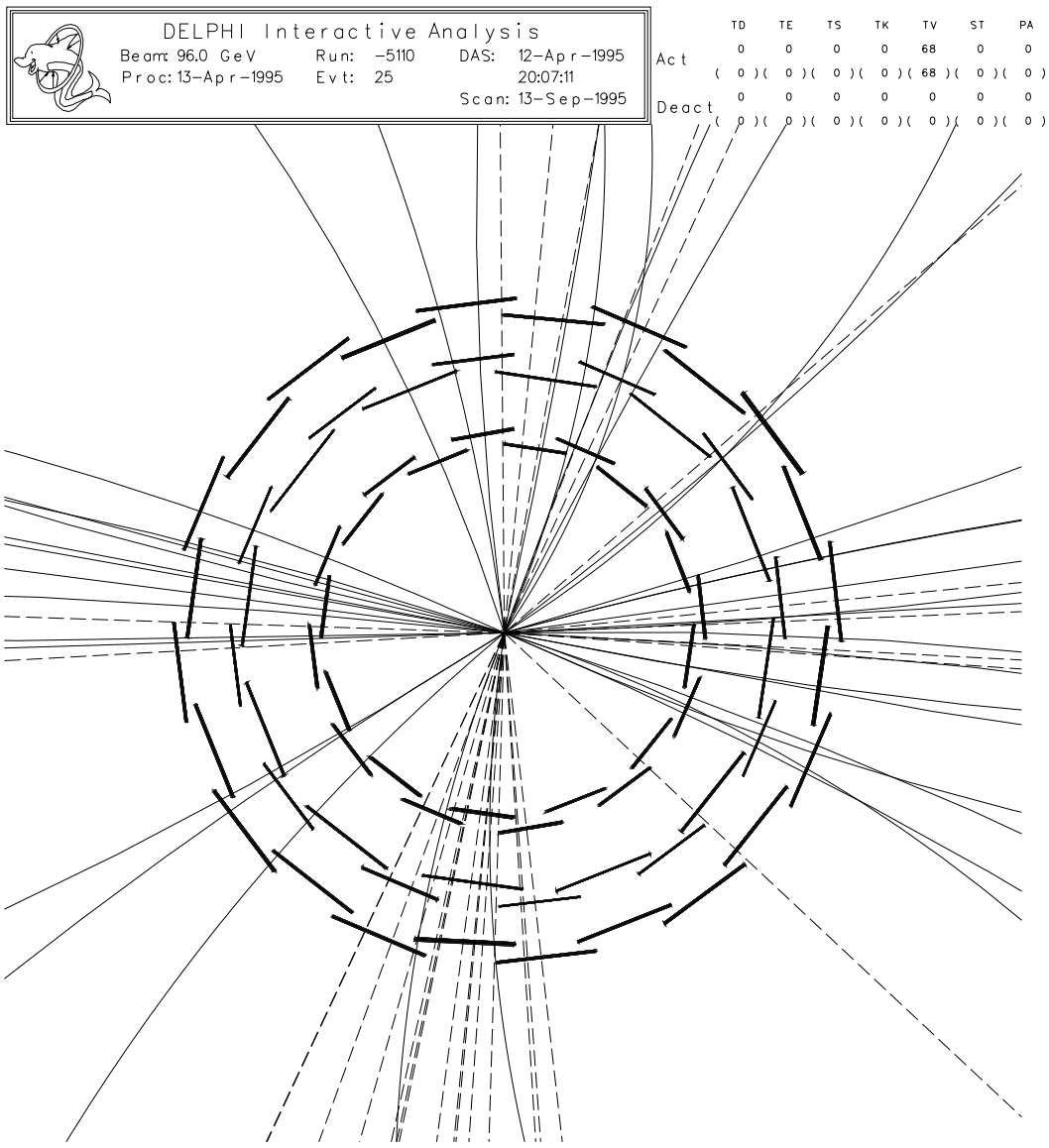

Figure 3.5: A generated $h^0A^0 \to b\bar{b}b\bar{b}$ event as seen in the DELPHI VD. $E_{cms} =$ 192 GeV and $m_{h^0} \approx m_{A^0} = 90$ GeV. All tracks are extrapolated into the Vertex, ie. no offsets are visible.

Chapter 4

Background Processes at LEP2

The main backgrounds for Higgs hunting at LEP2 are:

- $e^+e^- \rightarrow Z^0Z^0$
- $e^+e^- \rightarrow \gamma^*/Z^*/Z^0 \rightarrow f\bar{f}$
- $e^+e^- \rightarrow W^+W^-$

The Feynman diagrams for these processes are found in Figures 4.1 to 4.4. $e^+e^- \rightarrow W^+W^-$ has two important production modes at LEP2.

In about 75% of the $\gamma^*/Z^*/Z^0$ events a very hard ISR photon lowers the E_{cms} to the Z^0 mass, producing an on-shell Z^0. This process is called "Radiative return to Z^0", and whether the hard photon goes in the beam pipe or the barrel, it's easily removed by the cuts. In the remaining 25%, there's no hard ISR photon and the Z^0 is virtual (Z^*), with a mass of around E_{cms}. These events are a much more dangerous background to this analysis than the on-shell Z^0's. For simplicity the $\gamma^*/Z^*/Z^0$ background is referred to as the $f\bar{f}$ background throughout this analysis.

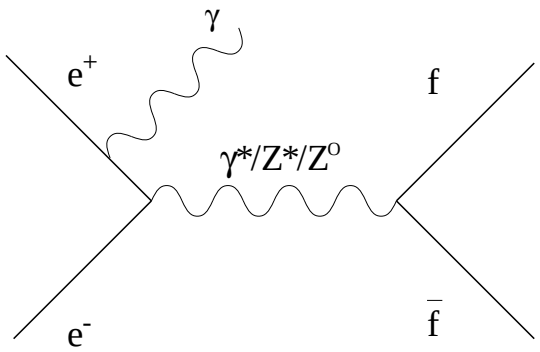

Figure 4.1: The $e^+e^- \rightarrow f\bar{f}$ annihilation diagram. In most cases at LEP2 the initial γ is very energetic and lowers the E_{cms} to the Z^0 mass.

$f\bar{f}$ is included here because it has a big cross section and sometimes produces more than 2 jets. These extra jets might come from gluon bremsstrahlung or wrong jet reconstruction. These cases can be very similar to the signal and demand special attention.

4.1 Background Cross Sections

The background cross sections are generally much bigger than the signal cross sections, making effective cuts essential to this analysis. Table 4.1 shows the cross sections for the main backgrounds at each energy analyzed in this thesis. They are calculated by Pythia[19] with ISR included.

E_{cms} (GeV)	$\sigma_{f\bar{f}}$ (pb)	$\sigma_{W^+W^-}$ (pb)	$\sigma_{Z^0Z^0}$ (pb)
175	175	15	0.5
192	134	18	1.2
205	111	18	1.5

Table 4.1: Total background cross sections.

4.2 Background Topologies

50% of the W^+W^- events decay to hadrons and none of them produce $b\bar{b}b\bar{b}$ events. Most of this background can therefore be removed by a strong B-tag[21] cut.

15% of the $f\bar{f}$ events are $b\bar{b}$ making this background harder to remove than W^+W^-. The $f\bar{f}$ events do however seldom produce the extra jets needed to make them similar to the signal.

The biggest background turns out to be Z^0Z^0 due to the irreducible $b\bar{b}b\bar{b}$ final state. Each Z^0 has a 15% branching ratio to $b\bar{b}$ and the chances for both Z^0's to decay into b pairs in the same event is 2.3%. These 2.3% are impossible[2] to distinguish from the signal and in addition some of the events where only 2 b's are produced pass the cuts.

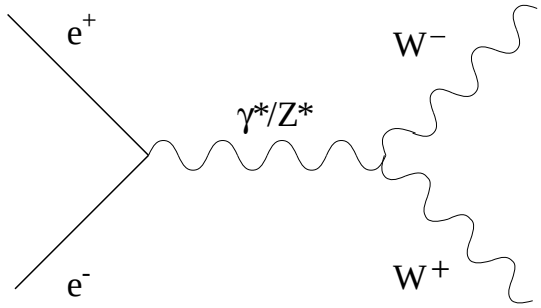

Figure 4.2: The $e^+e^- \rightarrow W^+W^-$ annihilation diagram.

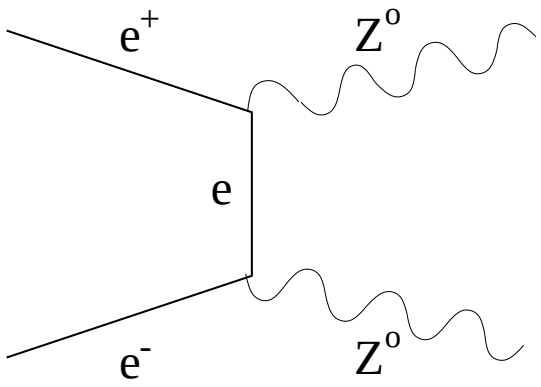

Figure 4.3: The $e^+e^- \rightarrow Z^0Z^0$ conversion diagram.

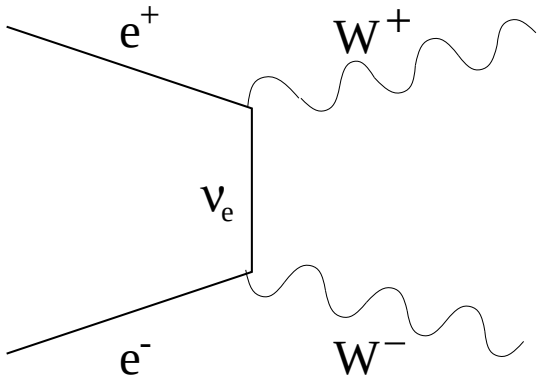

Figure 4.4: The $e^+e^- \rightarrow W^+W^-$ conversion diagram.

Chapter 5

Simulation of Events

At accelerators like LEP the processes studied are far too complex to be analyzed by hand like the bubble-chamber pictures were in the 50's and 60's. The rate and number of events have also increased a lot.

To spot Z^0's, W's and Higgs bosons, their decay products and topologies have to be known. (Seeing the bosons themselves is extremely unlikely due to their short average lifetimes of 10^{-20}s or less). When operating at LEP energies, the number of decay particles easily surpasses 50, giving infinite topology possibilities for the event. Every process still has a "most probable" topology though, with certain characteristics. Recognizing a process is therefore equivalent to finding its special topological attributes.

Unfortunately there are nearly always processes with similar topologies to the process looked for. These processes are called backgrounds (irreducible if totally similar). The process looked for is called the signal.

Because of the complexity of the events, special features of signals and backgrounds are often impossible to calculate or predict precisely. This is why good simulations are crucial to separate signal from background. By simulating events, one knows what one deals with and can easily compare signal and background system parameters. (The value of the parameters vary for each event, so one studies distributions from many events). A qualitative understanding of the processes is still needed to pick the interesting parameters to compare.

The parameter distributions showing the biggest differences between the signal and the background are chosen, and optimal cut values are found. These cuts are mostly simple, requiring a parameter to be above or below some constant value (found from simulation). Two-dimensional graphical cuts are also common if two parameters turn out to be correlated. This improves the efficiency of the cuts.

5.1 DELPHI Simulations

The raw data from DELPHI are processed by the DELANA[22] software which produces final DST's[23] (Data Summary Tapes). The DST's contain many separate events, and each event normally has many tracks. There are several program packages for reading DST's, this analysis uses PHDST[24].

Tracks are made from aligned detector hits and all detector hits are connected to a track (if possible). The information from the hits, connected to the track, is used for finding its energy, momentum, charge etc. The number of hits and their alignment determines the errors in these track parameters.

The procedure for simulating events is quite similar. Instead of getting raw data from DELPHI, physics simulator programs (PYTHIA[19] and JETSET[20] in this analysis) are first used to produce all the particles and their momenta. Then a detector simulator program (DELSIM[25]) is used to simulate DELPHI's response to the event. The data from DELSIM is of the same format as real

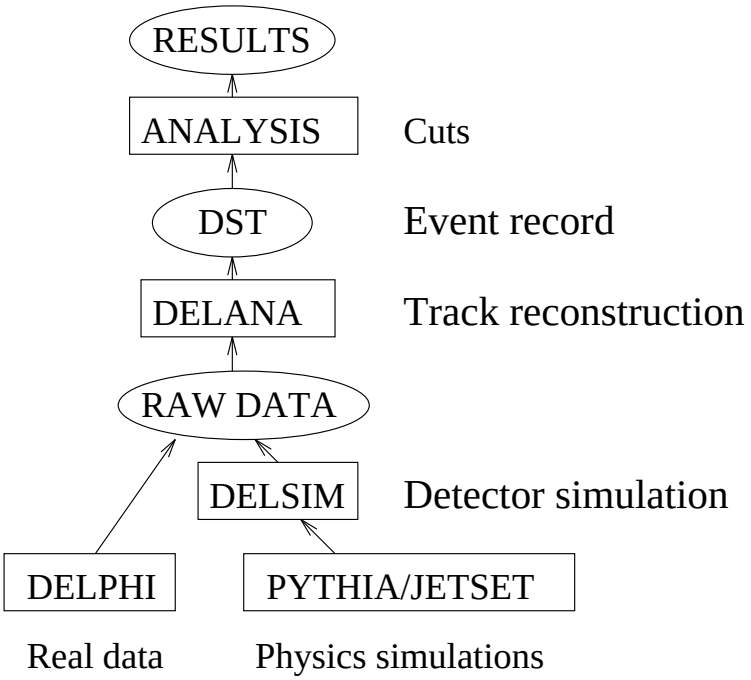

Figure 5.1: Data processing at DELPHI. Pythia, Jetset, Delsim and Delana are all computer programs.

DELPHI data and is analyzed in the same way.

Simulating and analyzing data is very time consuming, so data straight from the physics simulator are often used to get a qualitative impression of which cuts to use. Most cuts in this analysis are obtained in this way, straight from PYTHIA data. Since a lot of information and resolution is lost in the detector, full simulations are still needed for the final cuts.

Chapter 6

Analysis and Cuts

As mentioned in earlier Chapters, the main topology of a h^0A^0 event is $b\bar{b}b\bar{b}$. A significant excess of these events at LEP2 will therefore lead to the conclusion that a Higgs signal is seen.

The different cut parameter distributions in this Chapter are presented for ($E_{cms} = 192$ GeV): $f\bar{f}$, W^+W^-, Z^0Z^0, h^0Z^0 and h^0A^0 with $m_{A^0} = 80$, $m_{h^0} = 78$ GeV. Most of the distributions are quite similar for $E_{cms} = 175, 205$ GeV, and other m_{h^0}, m_{A^0} combinations. Distributions for 175 and 205 GeV are presented where necessary. The cuts are optimized for a mixture of all the available h^0A^0 datasets (Table 7.1), but only $m_{A^0} = 80$, $m_{h^0} = 78$ GeV is presented here for simplicity. The cuts aren't based on the h^0Z^0 signal at all, but the h^0Z^0 cut parameter distributions are shown for clarity. The h^0 mass used in the h^0Z^0 signal is 80 GeV, since 78 GeV data aren't available. The 2 GeV difference is negligible.

The efficiency of the h^0Z^0 search is increased to 20%(tripled) by expanding it from a $b\bar{b}b\bar{b}$ search to a $b\bar{b}q\bar{q}$ search. This is done by using mass reconstruction techniques[26] to check if the invariant mass of the $q\bar{q}$ pair matches that of the Z^0. Details of the $b\bar{b}q\bar{q}$ search at DELPHI are found in Ref. [2].

The mass reconstruction technique has its limitations though. When m_{h^0} is around m_{Z^0} the Z^0Z^0 background becomes very big, and when dealing with h^0A^0 the many possible mass combinations make things quite complicated. In addition, at high $\tan\beta (> 30)$ the width of the h^0 and A^0 bosons becomes significant. (The width of both bosons becomes $\sim$ 10 GeV at $\tan\beta = 60$). This might make it very hard to find peaks in the invariant mass distributions of a h^0A^0 search.

Should a h^0A^0 signal be seen in the $b\bar{b}b\bar{b}$ channel, determining the h^0 and A^0 masses will be urgent, so some sort of mass reconstruction analysis must be done. An analysis of this kind treating a few m_{A^0}, m_{h^0} points and operating at efficiencies around 20% is presented in Ref. [2].

To make a complete and optimized Higgs search, the different analyses for h^0A^0 and h^0Z^0 must be combined, which is partly done in Ref. [2].

All the available data at $E_{cms} = 192$ GeV (see next chapter for details) are used throughout this chapter. However, to remove leptonic events from the background distributions, only events with 10 or more tracks are presented in the distribution plots. These leptonic events are often neutrino events, with zero tracks, creating uninteresting peaks in the extremities of the distribution plots. In addition, the M1 vs. M2 scatter-plot (Fig. 6.12) only has 1000 of each background to limit the number of points on the plot.

The efficiencies of the cuts are nearly similar for all energies if other distributions (175, 205 GeV) aren't mentioned or discussed.

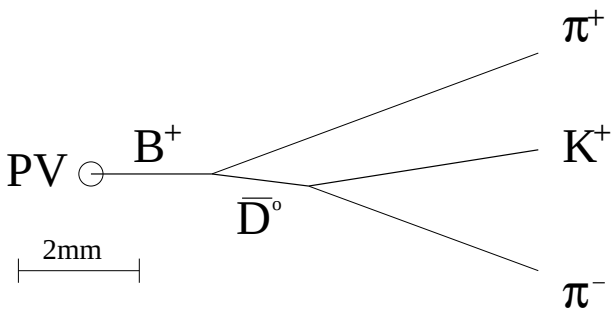

Figure 6.1: A typical B decay. PV is the Primary Vertex. The B^+ decay generates a secondary vertex.

6.1 The Quest for $b\bar{b}b\bar{b}$ Events

The most important tool for selecting B-events is the *B-tagging* [21]. This is however not enough to remove the background sufficiently. Additional properties of the event have to be examined to remove all of the reducible background, such as; the number of jets and B-jets in the event, deposits in the electromagnetic calorimeters, energy of the most energetic jet, conservation of momentum and energy in the event, and finally a look at invariant masses. This Chapter contains thorough information on all these properties of signal and background, and the cuts used in the analysis.

6.1.1 B-Tagging

The b-quarks, after being pair produced by h^0 or A^0 decays, pick up seaquarks to form B-hadrons. Since these B-hadrons contain a b-quark they have "bottomness". Strong decays require conservation of bottomness, energy and mass, and the B-hadrons have no such decay modes available. This forces them to decay through a flavour changing current, or weak decay. The same thing happens when h^0, A^0 or Z^0 decays to c or s-quark pairs creating charmed or strange hadrons. All these hadrons have different average lifetimes, which can be used to distinguish them. For example, the strange mesons (K's) have average lifetimes of $\approx 10^{-8}$s ($K^0_s \approx 10^{-10}$s), while the charmed mesons (D's) have lifetimes between 0.5 and $1 * 10^{-12}$s. The bottom mesons (B's) have mean lifetimes of $\approx 1.5 * 10^{-12}$s. All these lifetimes are picked from Ref. [3], and are typical for weak decays.

When these energetic mesons decay, a multitude of secondary particles is created. These, in addition to the fragmentation particles produced directly at the vertex, form the jets (Fig. 3.4). The lifetime of the original meson determines the displacement of the jet vertex, and heavy mesons have "broader" jets than light mesons. In Fig. 6.1 a B decay is shown, with the secondary vertex (jet origin) beginning where the B decays. PV is the primary Vertex, ie. the collision

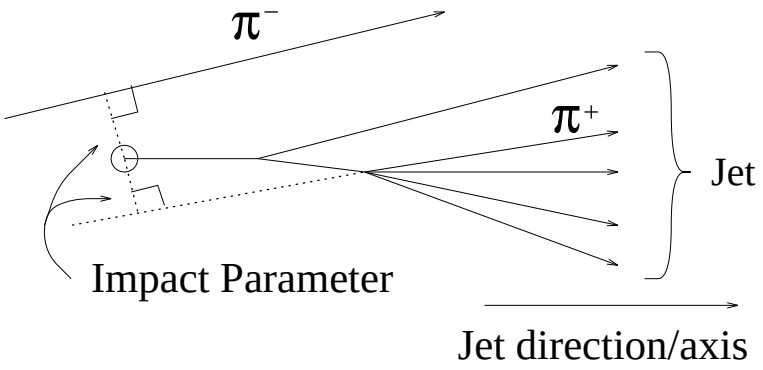

Figure 6.2: Description of the Impact Parameter.

point of the e^+ and e^-.

The B-tagging method[21] used in this analysis, is heavily based on the impact parameter. The impact parameter of a track is the shortest distance between the PV and the extension of the track past the PV. Fig. 6.2 shows the impact parameter of a track belonging to a jet (π^+) and of a track not belonging to the jet (π^-). The π^+ has a positive impact parameter because the extension of the track passes "in front" of the PV. If the π^- passing the jet is mistaken as part of the jet, it gets a negative impact parameter because it passes "behind" the PV. Another way to determine the sign of the impact parameter is to look at the angle between the direction of the jet axis and the impact parameter. Impact parameters with angles less than 90°, to the jet axis, have positive impact parameters, and IP's with higher angles are negative.

In an event where all tracks are from the primary vertex, the impact parameters are distributed around zero due to the limited resolution of the detector, multiple scattering and errors in the track reconstruction. The idea is to use this distribution to find a track's probability of being from the PV. When combining these track probabilities for a group of tracks, their combined chance of being from the primary vertex can be studied.

Making an impact parameter distribution with tracks only originating from the PV is the first goal. Unfortunately, all real samples are contaminated by tracks not originating from the primary vertex, so a trick is needed. Somehow the distribution of positive IP's must be obtained, because only tracks with positive IP's are studied in the final analysis (tracks with negative IP's are ignored). The contamination in the samples are mostly correctly reconstructed tracks from secondary vertices (like B-jets), having positive impact parameters. The contamination is therefore concentrated on the positive side of the IP distribution. If one assumes that the distribution of the pure sample (only tracks originating from the PV) is equal for both negative and positive impact parameters, the negative

distribution can be flipped to make the positive distribution. A positive distribution function can therefore be produced directly from the negative distribution. This function is fitted to the negative distribution for LEP2, and its integral is normalized to one(Fig. 6.3). It's very dependent on the detector resolution and is therefore called the "resolution function". Only tracks with negative IP's between 0 and -2 mm are used to make this function. Tracks with smaller IP's than -2 mm are too badly reconstructed to be of any use.

To find the probability that a track originates from the primary vertex, $P(ip)$, the resolution function is integrated from the IP of the track, and up to 2 mm. Tracks with IP's above 2 mm are ignored. As seen in Fig. 6.3, these integrals drop rapidly for high impact parameters. Their values are always between 0 and 1, since the total integral of the resolution function is normalized to one.

After PV origination probabilities are calculated for a group of tracks (event, jet etc.), they are combined statistically into one single probability for that group. This combined probability is called the "N-track probability", and it tells the probability that the chosen group of tracks originate from the primary vertex ($0 \leq$N-track prob. ≤ 1). A small N-track probability means that most of the tracks examined probably aren't from the PV, ie. they are from secondary vertices, most likely B-mesons. In general, the N-track probability of an event is inversely proportional to the number of B-jets in it.

The N-track probability is calculated using this statistical formula:

$$P_N \equiv \Pi \sum_{j=0}^{N-1} \frac{(-\ln \prod)^j}{j!} \qquad \Pi \equiv \prod_{i=1}^{N} P(ip)$$

When only tracks with positive IP's are used (as in this analysis), P_N is called the positive N-track probability, or Probp.

The distributions of the positive N-track probability are found in Fig. 6.4. Fig. 6.5 shows the same distributions below 10^{-8}.

The chosen cut for Probp is:

- Probp$< 10^{-9}$ for all energies

This cut is extremely hard on non-B events, especially W^+W^- events.

The resulting percentage of events left, after only this cut, is found in Table 6.1.

6.1.2 Jet Reconstruction

To find out more about the event it's necessary to examine its jets and their characteristics. Two different algorithms are often used for jet reconstruction at e^+e^- colliders, JADE and LUCLUS. Both are part of the JETSET program package[20].

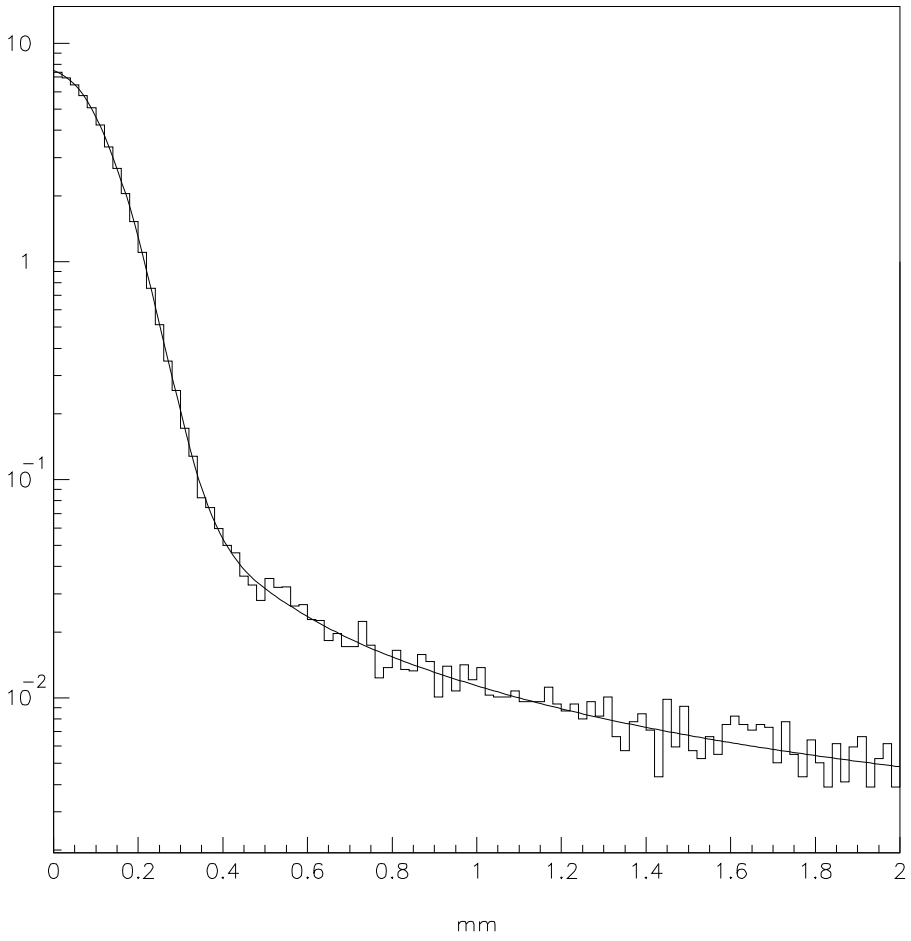

Figure 6.3: The distribution of the negative impact parameters between 0 and -2 mm, and the fitted resolution function. The negative distribution has here been flipped around the y-axis to simulate the positive distribution of tracks originating from the Primary Vertex.

Probp $< 10^{-9}$					
	h^0A^0	h^0Z^0	Z^0Z^0	ff	W^+W^-
% left	49.7	19.2	5.0	1.8	0

Table 6.1: Percentage of events left after the Probp cut, for the data at $E_{cms} = 192$ GeV.

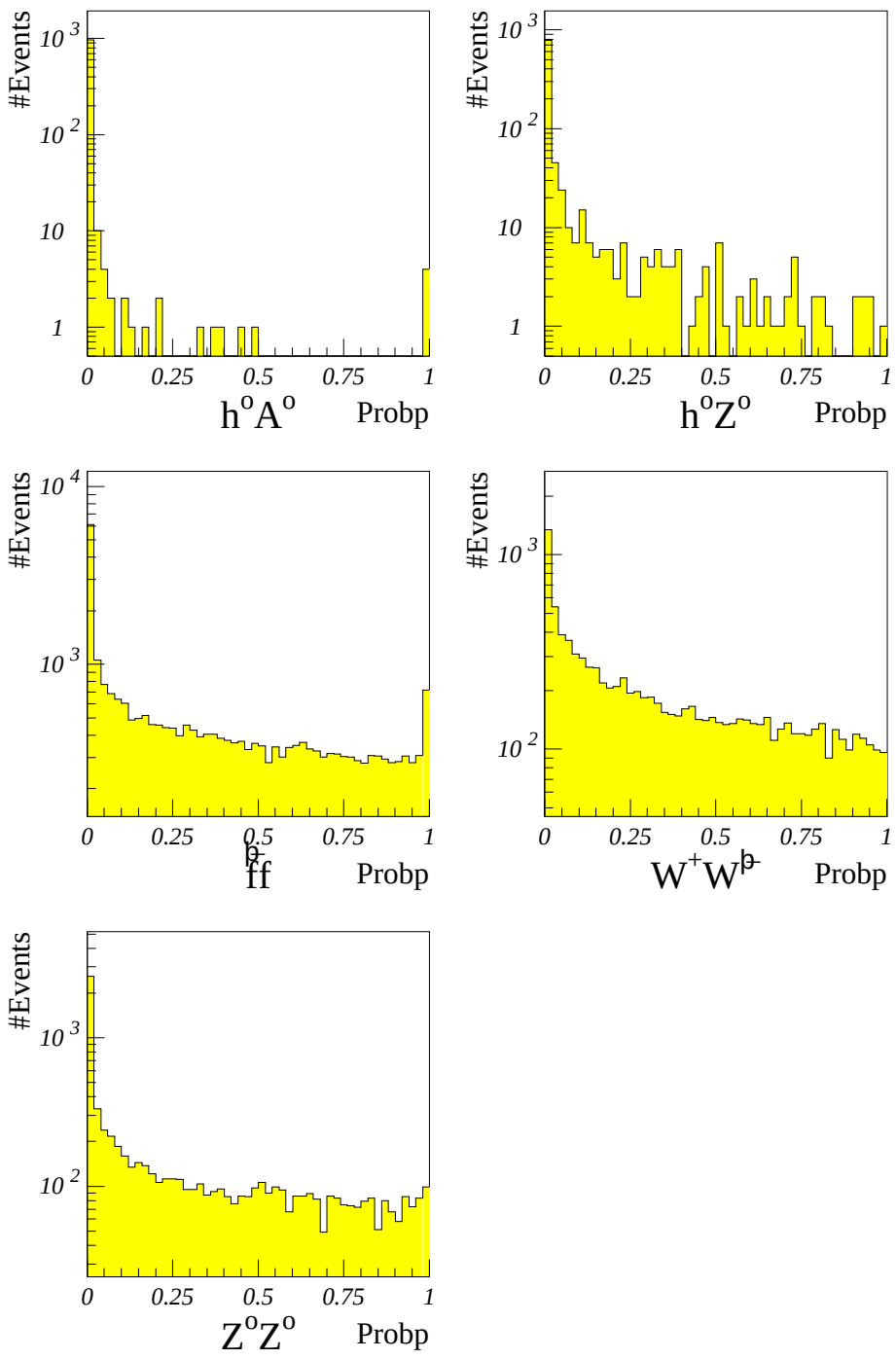

Figure 6.4: The positive N-track probability for the data at $E_{cms} = 192$ GeV.

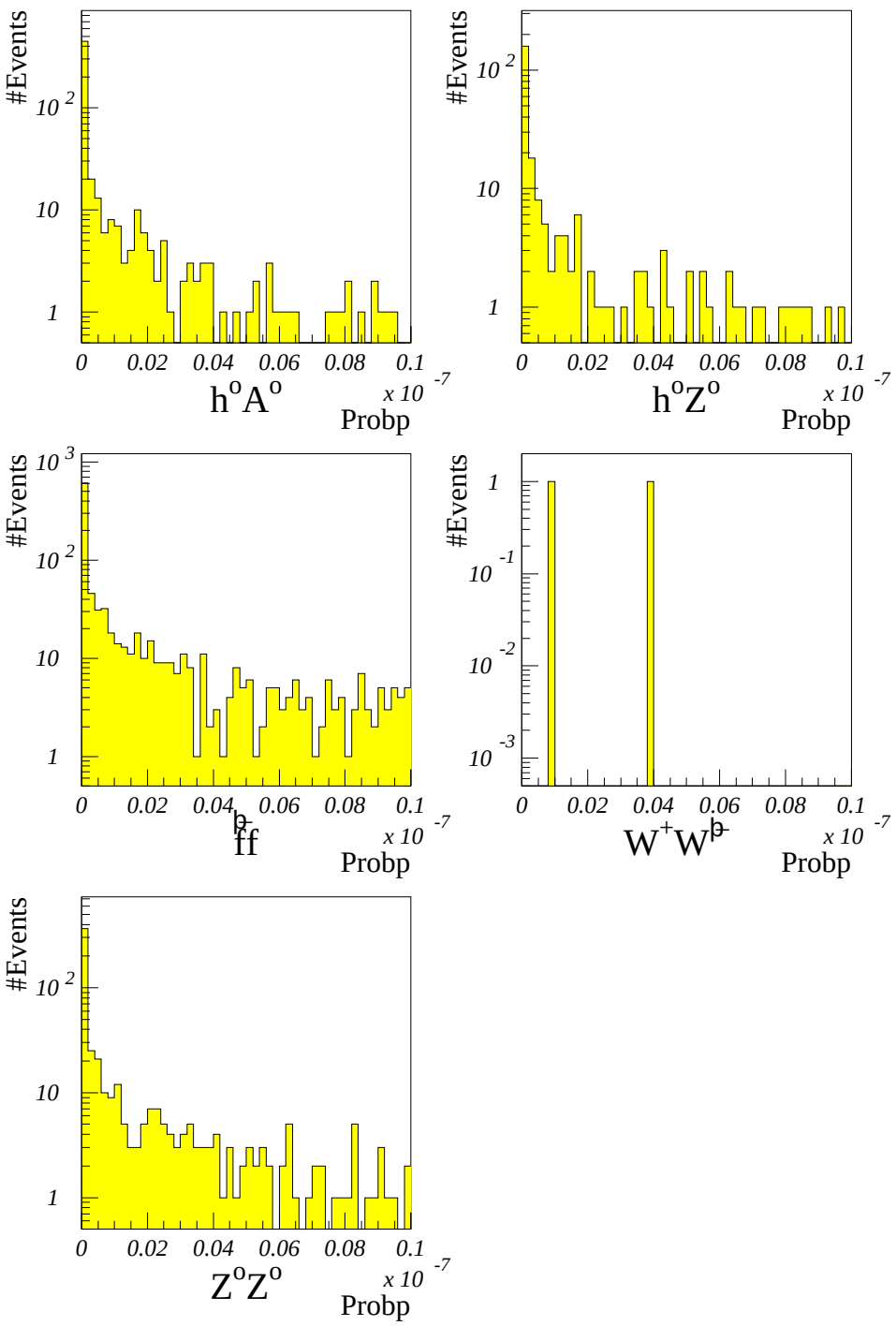

Figure 6.5: The positive N-track probability below 10^{-8} for the data at E_{cms} = 192 GeV.

The LUCLUS algorithm starts by picking the highest momentum particle as the first cluster (jet). Then it checks the d_{ij} values of the other tracks, ie. their angular distance, given by:

$$d_{ij} \approx \frac{|p_i \times p_j|}{|p_i + p_j|} \tag{6.1}$$

If this value is below a predetermined value, d_{join}, the tracks are connected, and their combined momentum (added vectorially) is treated as the new cluster. This process is repeated for the remaining unassigned tracks, until all tracks are assigned to a cluster, and all clusters are separated by at least d_{join}. A higher d_{join} produces therefore fewer jets. Isolated tracks often become their own cluster (jet) using this algorithm.

The only difference between JADE and LUCLUS is the way they calculate the angular distance between tracks. The distance measure for LUCLUS, d_{ij}, is given in Eq. (6.1), and the distance measure for JADE, y_{ij}, looks like this:

$$y_{ij} = \frac{2E_iE_j(1-\cos\theta_{ij})}{E_{vis}^2},$$

where E_{vis} is the total visible energy of the event. The JADE equivalent of d_{join} is called y_{join}.

The JADE algorithm is a little better at finding the right number of jets, whereas LUCLUS gives better jet directions and energies[27]. LUCLUS can still reproduce the right number of jets almost as good as JADE if a good d_{join} value is chosen. This is why LUCLUS is used throughout this analysis, except in the B-jet reconstruction, which is done internally in the B-tagging program package[21], using JADE with $y_{join} = 0.01$.

The best value for d_{join} depends mostly upon the energy, and for LEP2 energies, $d_{join} = 5$ GeV turns out to be a good choice [28]. Using the right d_{join} value is especially important for separating 2-jet and 4-jet events ($f\bar{f}$, $b\bar{b}b\bar{b}$).

The distributions of the number of jets, N_{jets}, are found in Fig. 6.6.

The chosen cut for N_{jets} is:

- $N_{jets} > 3$ for all energies

This cut removes a lot of $f\bar{f}$ events. The resulting percentage of events left, after only this cut, is found in Table 6.2.

6.1.3 B-Jets

As shown earlier, the signal topology is typically a $b\bar{b}b\bar{b}$ event, which is very rare among the background events. The next step, after jet reconstruction, is therefore to look for B-jets. These are often broad, many-particle jets, coming from a secondary vertex.

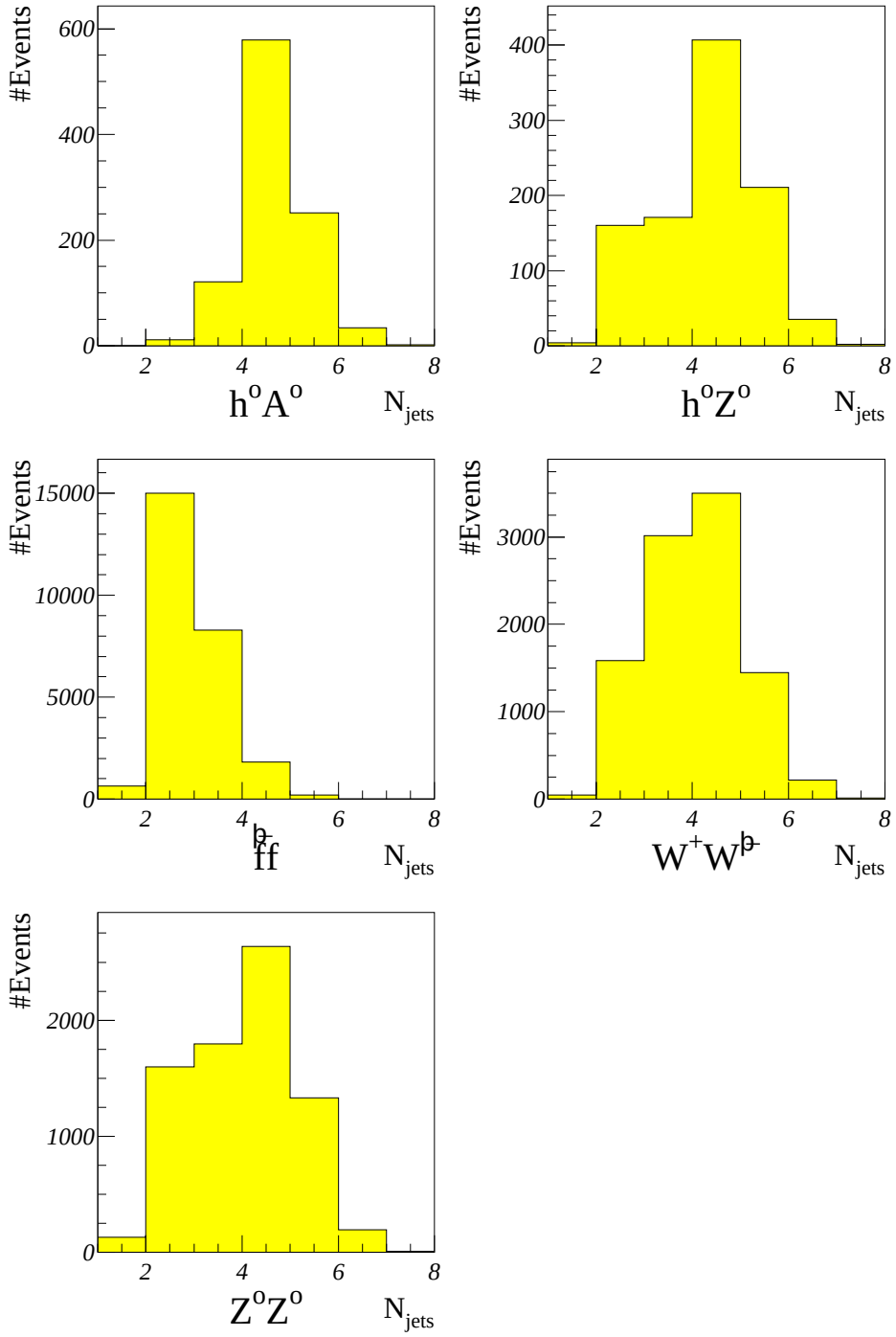

Figure 6.6: The number of jets in each event. Here shown for $E_{cms} = 192$ GeV.

$N_{jets} > 3$					
	h^0A^0	h^0Z^0	Z^0Z^0	ff	W^+W^-
% left	86.8	65.5	48.3	5.1	47.5

Table 6.2: Percentage of events left after the N_{jets} cut, for the data at $E_{cms} = 192$ GeV.

Each jet identified by JADE is required to satisfy three criteria, to be classified as a B-jet:

1. The combined Positive N-track Probability (Probp) of all tracks in the jet must be less than 0.05, because broad and offset jets have small Probp's.

2. The number of tracks in the jet must be equal to, or higher than 3, because B-jets often have high multiplicity.

3. The Energy of the jet must be equal to, or higher than 5 GeV, because jets with less energy are poorly defined at LEP2.

Many different values were tried to optimize the above criteria.

This analysis uses a rather simple approach to classify B-jets, more sophisticated methods are under development. These methods incorporate particle types and charges.

The number of jets in each event, passing these criteria, reflects the true number of B-jets in the event quite well.

The distributions of the number of B-jets, N^B_{jets}, are found in Fig. 6.7. The internal jet reconstruction in the B-tagging program package[21] is used, ie. JADE with $y_{join} = 0.01$.

The chosen cut for N^B_{jets} is:

- $N^B_{jets} > 2$ for all energies

This cut is very hard on all backgrounds. The resulting percentage of events left, after only this cut, is found in Table 6.3.

$N^B_{jets} > 2$					
	h^0A^0	h^0Z^0	Z^0Z^0	ff	W^+W^-
% left	54.8	14.9	3.5	0.3	0.3

Table 6.3: Percentage of events left after the N^B_{jets} cut, for the data at $E_{cms} = 192$ GeV.

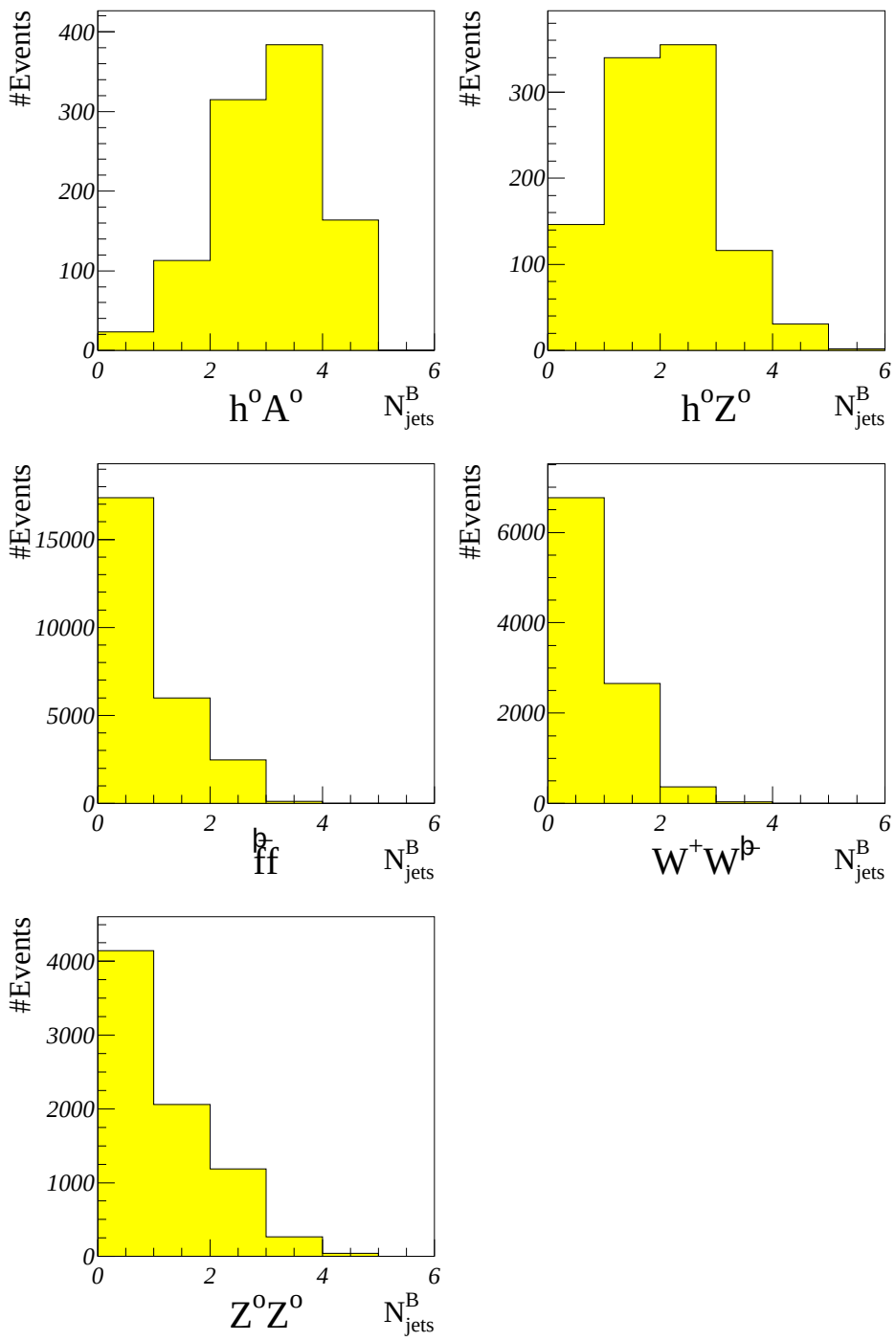

Figure 6.7: The number of B-jets in each event, for the data at $E_{cms} = 192$ GeV.

6.1.4 The Energy of the Main Jet

When h^0 and A^0 are produced together at LEP2, nearly all the available energy is "absorbed" by them and make up their masses, especially in the $m_{h^0} + m_{A^0} \approx E_{cms}$ region. This leaves the Higgs bosons with no momentum. These "resting" bosons decay into $f\bar{f}$ (mostly $b\bar{b}$), each fermion with equal momentum and energy (from conservation). Each boson should therefore produce two back-to-back jets with equal energy ($\frac{1}{2}m_{boson}$).

For lower mass Higgs bosons ($m_{h^0} + m_{A^0} < E_{cms}$), there's enough energy left after the h^0A^0 production to give them a considerable momentum. When these boosted bosons decay, the jets have different energies in the detector rest frame. The forward jet being the most energetic. The case of both jets being perpendicular to the boost direction, and thereby getting equal energy, is very rare since these Higgs bosons decay isotropically.

The energy of the jet with highest momentum (E_1) is therefore $\sim \frac{1}{2}m_{boson}$ in the $m_{h^0} + m_{A^0} \approx E_{cms}$ case, and higher when $m_{h^0} + m_{A^0} < E_{cms}$. This produces narrower E_1 distributions in the first case than in the second. E_1 in case one also tends to be a little lower.

Since E_1 depends on the center-of-mass energy, its distribution is shifted towards higher energies for $E_{cms} = 205$ GeV, and lower energies for $E_{cms} = 175$ GeV (compared to 192 GeV). This is why different cuts are needed for each energy.

For the Z^0Z^0 and W^+W^- backgrounds, the situation is quite similar. This is however not the case for the $f\bar{f}$ background. Here there's a very boosted system if a hard γ is radiated (radiative return to Z^0), or two jets with high momenta if no hard γ is radiated. The quarks creating these jets might also radiate gluons to create more jets.

All these different possibilities result in a broader E_1 distribution for $f\bar{f}$ than for all the other signals and backgrounds, Fig. 6.8. While the low-energy tail in the $f\bar{f}$ distribution is quite harmless to this analysis, the high-energy tail contains some dangerous background events. The cut is done in the high end of the E_1 distribution to remove this high-energy tail.

The E_1 distributions are shifted towards higher energies for higher center-of-mass energies. This effect isn't very interesting or surprising, so distributions are only shown for 192 GeV, like in the previous cuts.

To show how higher Higgs masses tightens and shifts the h^0A^0 E_1 distribution, $m_{A^0} = 90$, $m_{h^0} = 87$ GeV ($E_{cms} = 192$ GeV) has been included in Fig. 6.8. The variations for h^0Z^0 are much smaller, since m_{Z^0} is constant.

The distributions of E_1 (two h^0A^0 combinations) are found in Fig. 6.8.

The chosen cut for E_1 is:

- $E_1 < \frac{14}{17}E_{cms} - 83$ GeV

The resulting percentage of events left, after only this cut, is found in Ta-

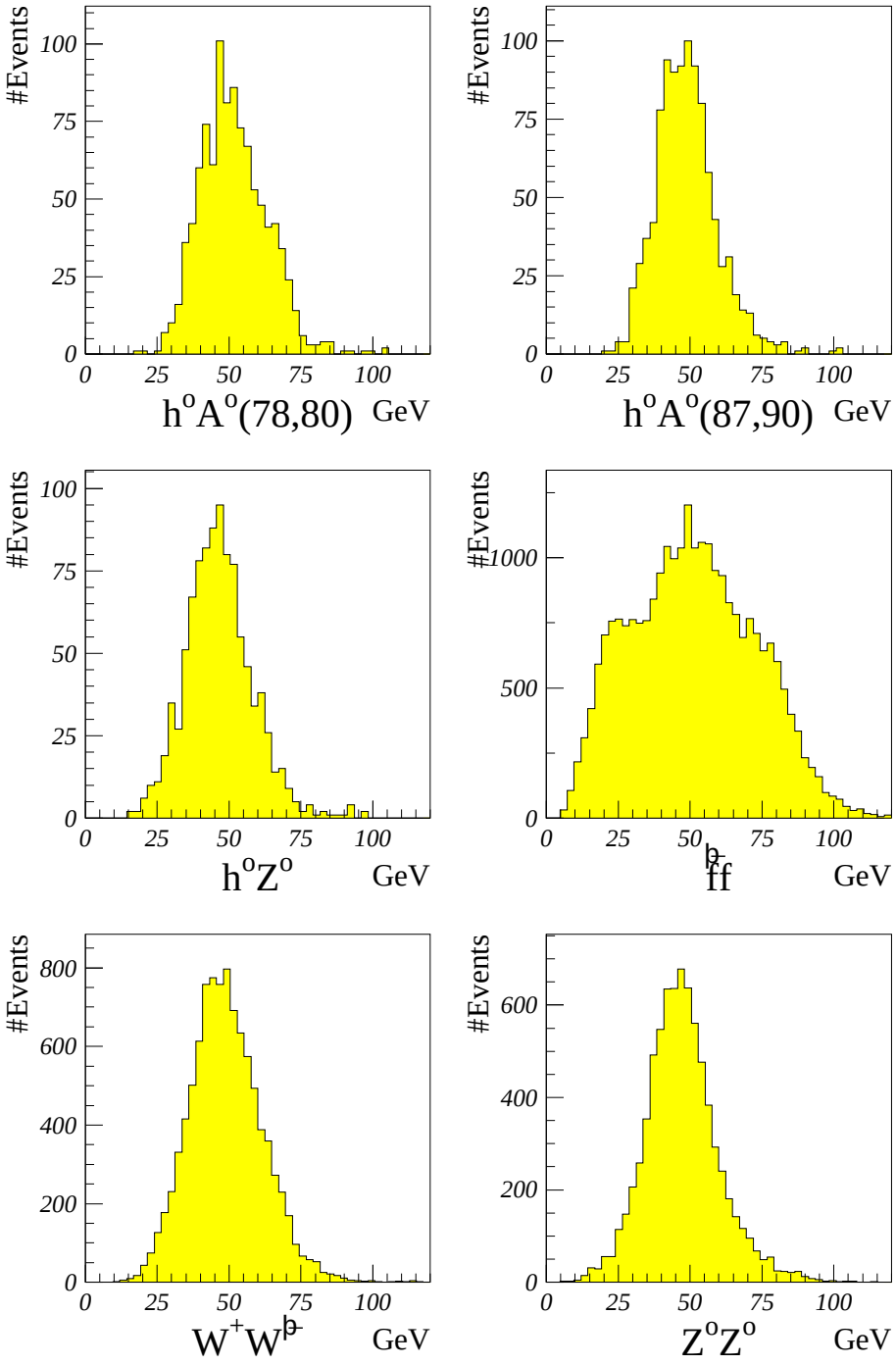

Figure 6.8: The energy of the jet with highest momentum. Here shown for the data at $E_{cms} = 192$ GeV.

ble 6.4. The extra h^0A^0 mass combination ($m_{A^0} = 90$, $m_{h^0} = 87$ GeV) isn't included in this table.

$E_1 < 75$ GeV					
	h^0A^0	h^0Z^0	Z^0Z^0	$f\bar{f}$	W^+W^-
% left	97.7	98.2	97.4	88.0	97.6

Table 6.4: Percentage of events left after the E_1 cut, for the data at $E_{cms} = 192$ GeV.

6.1.5 Electromagnetic Deposits

One of the most significant features of the $f\bar{f}$ background is a hard γ (or several) often seen together with the fermions, in the event. This is the Initial State Radiation photon(s).

These photons mostly leave the detector undetected, through the beam pipe. This is seen as lost z-momentum (beam pipe direction) and lost energy in the event. Few jets are produced, and the observed momentum and energy is badly conserved in the event. These cases are removed by other cuts in this analysis.

A few of the photons have bigger θ angles, ie. they pass through the electromagnetic calorimeters of DELPHI (not the beam pipe). θ is the angle between the tracks and the beam pipe. At low θ the γ's are seen in the STIC, which is located near the beam pipe on both sides of the interaction point, Fig. 1.1. At higher θ's they're seen in the Forward EM Calorimeter (FEMC), located in the end cap. And at the highest θ's they're detected by the High Density Projection Chamber (HPC), located in the barrel.

In addition to the γ's leaving big energy deposits in the EM calorimeters, the $f\bar{f}$ might be e^+e^-, which also leaves big EM calorimeter deposits. Especially if no initial ISR photon is radiated (e^+e^- shares all the energy).

The W^+W^- and Z^0Z^0 backgrounds might also produce hard $e^\pm$'s through direct decays ($W^\pm \rightarrow e^\pm \nu_e$, $Z^0 \rightarrow e^+e^-$). These hard γ's and $e^\pm$'s coming from the backgrounds aren't seen in the signal, and their energies rise with higher E_{cms}.

Fig. 6.9 shows the distributions of Emcamax, the biggest energy deposit in the HPC or FEMC. The high-energy γ's and $e^\pm$'s are only seen in the backgrounds. This cut removes this high-energy tail. These distributions are stretched out for $E_{cms} = 205$ GeV and shrunk for $E_{cms} = 175$ GeV, so different cuts are needed for each energy.

Emcamax doesn't include the STIC, since all the background events with high-energy STIC deposits are removed by other cuts. This isn't the case for the HPC and FEMC.

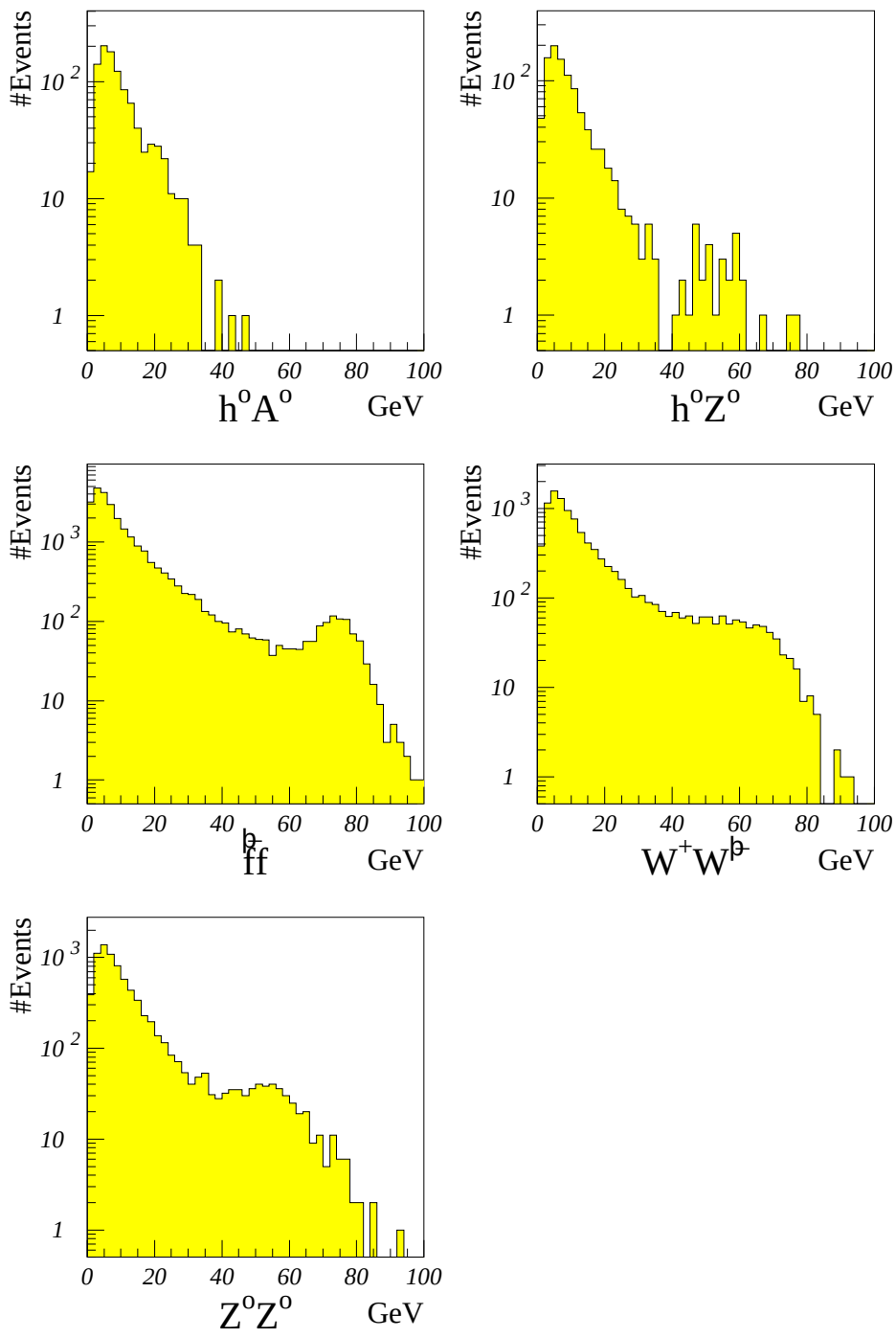

Figure 6.9: The biggest energy deposit in the EM calorimeters. Here presented for the data at $E_{cms} = 192$ GeV.

The chosen cut for Emcamax is:

- Emcamax$< 0.22 E_{cms}$

The resulting percentage of events left, after only this cut, is found in Table 6.5.

Emcamax$<$ 42 GeV					
	h^0A^0	h^0Z^0	Z^0Z^0	$f\bar{f}$	W^+W^-
% left	99.8	96.9	93.1	90.5	89.0

Table 6.5: Percentage of events left after the Emcamax cut, for the data at $E_{cms} = 192$ GeV.

6.1.6 Conservation of Momentum and Energy

One of the most fundamental principles in physics is conservation of momentum and energy. This of course also applies to the events studied at LEP2.

If p and E are badly conserved in an event this indicates that high-momentum tracks have gone undetected, or neutrinos are involved. High-energy neutrinos might come from all the backgrounds, and high-momentum tracks going undetected are mostly seen in $f\bar{f}$ events (γ's going down the beam pipe).

To only examine conservation of both momentum and energy, combining all tracks is the best. The routine used here (PUFIT[26]) is however created to handle many kinds of situations, like reconstructing invariant masses of jet systems etc. , so all events are first reconstructed into 4 jets, using LUCLUS.

Forced jet reconstruction into 4 jets isn't very different from normal reconstruction. First LUCLUS picks out 4 "main" tracks, then all other tracks are connected to their nearest main track (jet). The distance measure is the same as in the jet reconstruction Section, Eq. (6.1). After all tracks have been assigned to a jet, the new jet direction (momentum) is calculated. Each track is then reassigned to its nearest jet (using the last calculated jet directions). This procedure is iterated until no tracks change jets during reassignment.

These 4 jets are then treated as single tracks, and a fit for conservation of p and E in the event is performed. Distributions of χ^2's of this fit (χ^2_{tot}) are found in Fig. 6.10. Comparing them directly is possible since all the fits have the same number of degrees of freedom.

The difference between the Z^0Z^0 and W^+W^- backgrounds reflects that $W^\pm$ decays more often to neutrinos than Z^0.

The difference between h^0Z^0 for $m_{h^0} = 80$ and $m_{h^0} = 90$ GeV, both shown in Fig. 6.10, arise from the fact that these events have different topologies. The case

with $m_{h^0} = 80$ tend to have more jets in the forward direction, ie. more tracks along the beam pipe, causing a worse (bigger) χ^2_{tot}. The same effect isn't seen in h^0A^0.

The chosen cut for χ^2_{tot} is:

- $\chi^2_{tot} < 0.27 E_{cms}$

The resulting percentage of events left, after only this cut, is found in Table 6.6. The h^0Z^0 percentage is for $m_{h^0} = 80$ GeV.

$\chi^2_{tot} < 52$					
	h^0A^0	h^0Z^0	Z^0Z^0	ff	W^+W^-
% left	89.8	62.2	48.5	19.5	44.2

Table 6.6: Percentage of events left after the χ^2_{tot} cut, for the data at $E_{cms} = 192$ GeV.

6.1.7 Invariant Masses

The last cut used in this analysis looks at the invariant masses of the two jets produced by a forced 2-jet reconstruction.

The invariant masses of these 2 jets are calculated by LUCLUS, using the transverse momentum in the jet. The mass of the jet with biggest momentum is baptized M1, and the mass of the other jet is called M2.

The jet topology for all signals and backgrounds can roughly be summed into 3 different cases, illustrated in Fig. 6.11. Case 2 and 3 applies to the $f\bar{f}$ background and case 1 to the signals and the rest of the backgrounds. $f\bar{f}$ comes from an initial γ^*, Z^* or Z^0, and the rest are from 2 initial bosons. I_1 and I_2 are jets coming from initial particle 1 or 2.

Since all the bosons in the signals and backgrounds are heavy (80–90 GeV), and are produced in pairs, little of the E_{cms} is left for giving them momentum. The jets produced by these "resting" bosons are therefore back-to-back, as in case 1, Fig. 6.11. When forcing case one into 2 jets, the jets on the left side become one, and so does the jets on the right side. These 2 jets, with masses M1 and M2, are nearly always made up of one I_1 jet and one I_2 jet.

In most cases the jet reconstructed from I_1 and I_2 on one side (left, in Fig. 6.11), has higher invariant mass (spread) than the jet on the other side. The jet with biggest spread and invariant mass (left) is often the jet with biggest momentum. This is why M1 tend to be bigger than M2.

In case 2 ($f\bar{f}$) the γ often goes into the beam pipe, and only two jets remain. LUCLUS reconstructs these, and since they're not mixtures of several jets, their

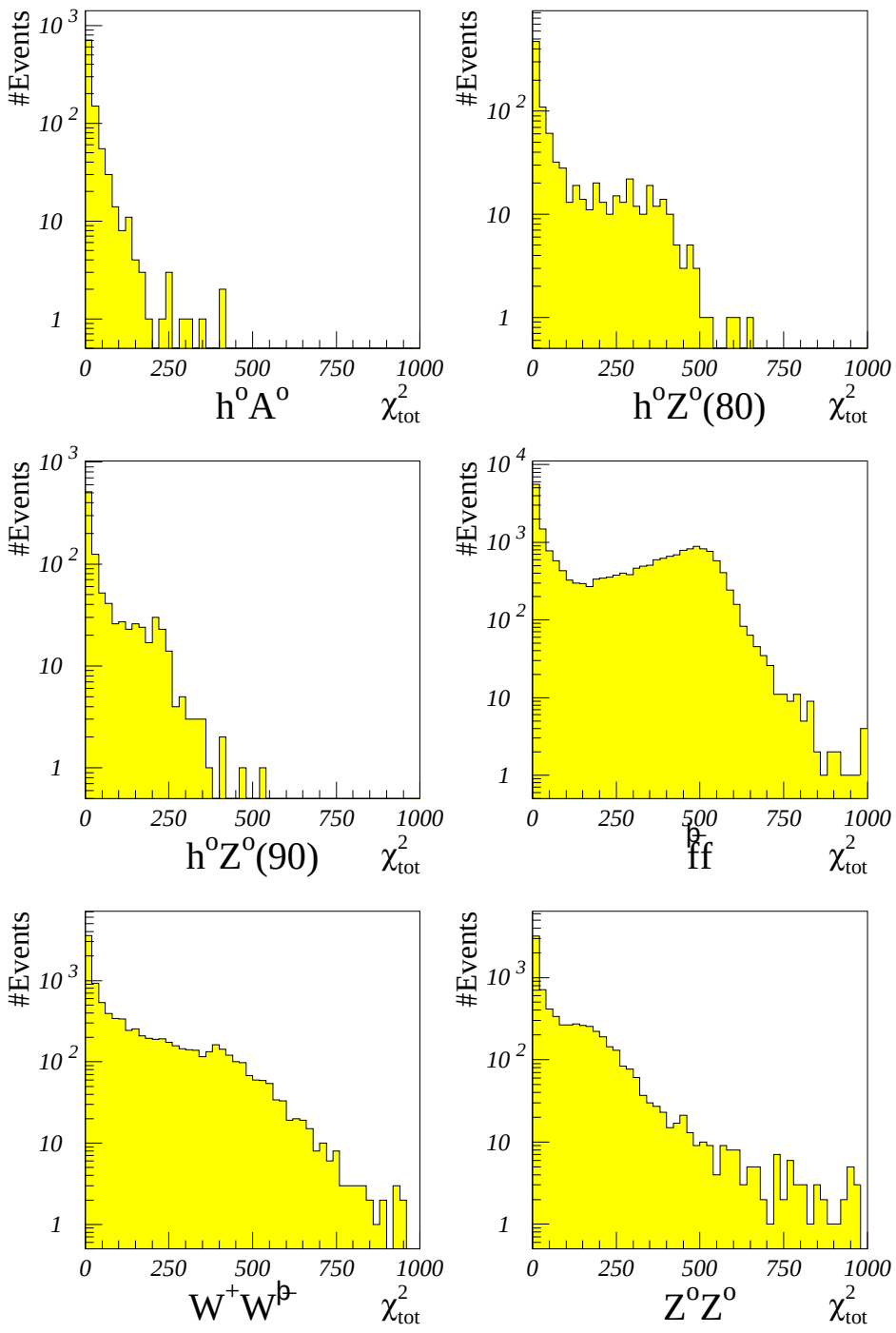

Figure 6.10: The χ^2 of the conservation of p and E fit. Shown for the $E_{cms} = 192$ GeV data.

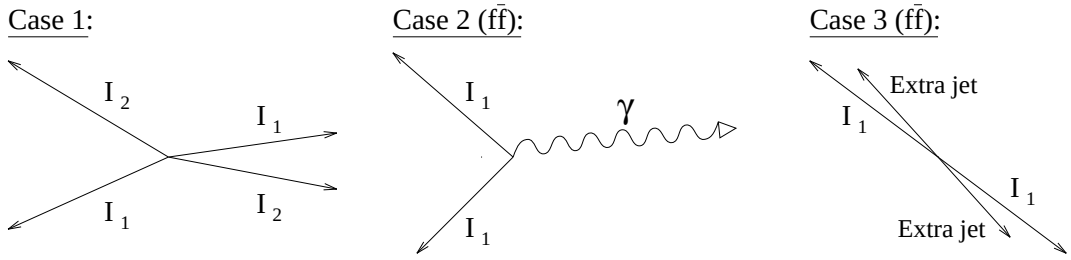

Figure 6.11: The 3 most common topology cases.

spread and masses are small compared to those of case 1. These events (case 2) are however removed by other cuts.

The real strength of this M1 vs. M2 cut is that it removes many case 3 events that survive all the other cuts. These are $f\bar{f}$ events where no hard ISR γ is emitted. The extra jets in Fig. 6.11 may come from gluon bremsstrahlung, or jet splitting arising from bad jet reconstruction. Since the gluons are radiated by the $f\bar{f}$ pair, their momenta tend to be aligned to those of the initial fermions (I_1). This often gives the 2 jets reconstructed from case 3 less invariant mass than those reconstructed from case 1.

The distributions of M1 versus M2, are shown in Fig. 6.12. The cut is shown as a line, everything outside it is removed. It's done graphically because this is more efficient than separate cuts, which would be the same as using a square box in the graphical cut. The cut is optimized for a mixture of all the available h^0A^0 datasets at each energy (like all the other cuts), and is mainly introduced to deal with case 3, $f\bar{f}$ background.

The h^0A^0 distribution is made up entirely of case 1 events.

The h^0Z^0 plot has a concentration of events at low M1 and M2. These are events where Z^0 decays to $\nu\bar{\nu}$ (20%), giving the events only 2 jets (from h^0). This produces the small M1's and M2's, as in case 2 events. The 10% of the events where Z^0 decays into charged leptons are also found in the lower left corner, although a little smeared by the leptons.

The $f\bar{f}$ plot has a huge concentration of events in the lower left corner, these are the case 2 events (75%). The rest are case 3 events, and their distribution has a great impact on the shape of this graphical cut.

The W^+W^- background produces 2 charged leptons and 2 ν's in around 10% of the cases. These are found in the lower left corner if they have 10 tracks or more. Around half of the remaining W^+W^- events produces 2 quarks, 1 charged lepton and 1 ν. The 2 quarks are from the same W. The charged lepton is added to one of the jets, raising the invariant mass a little. This is why the lump at low M1 and M2 is more smeared for W^+W^- than for h^0Z^0. The last 50% of the W^+W^- events are standard case 1 events with 4 quarks.

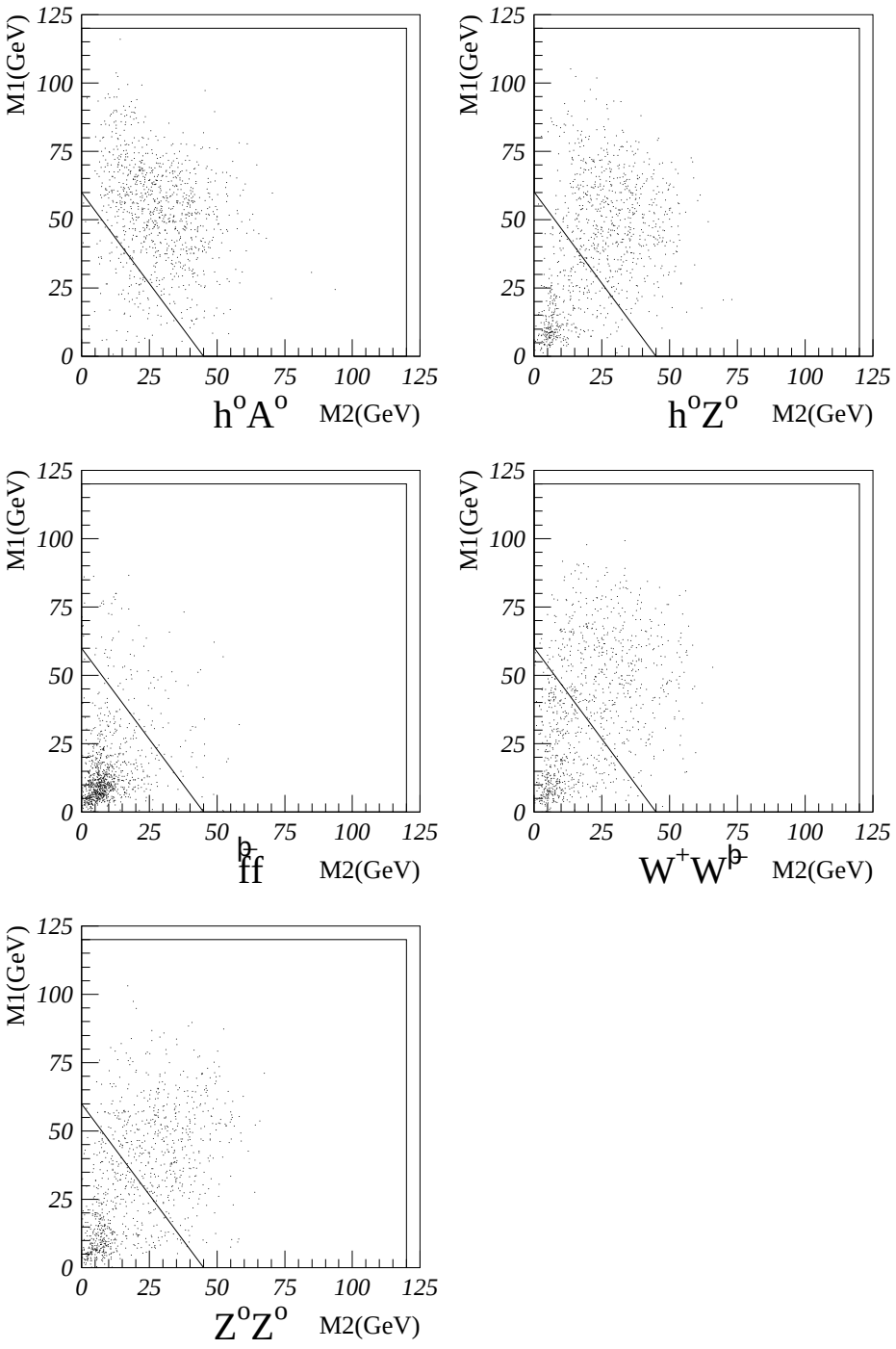

Figure 6.12: The graphical cut in the M1 vs. M2 plots. Here shown for the $E_{cms} = 192$ GeV data.

The Z^0Z^0 background creates 4 leptons in 10% of the cases. These are found in the lower left corner if they have more than 9 tracks. 30% of the remaining Z^0Z^0 produce $q\bar{q}\nu\bar{\nu}$. These events are also found in the low mass corner. 16% of the remaining Z^0Z^0 include 2 charged leptons and 2 quarks. These also have small M1 and M2, but they'll smear the lump, as in W^+W^- and h^0Z^0. The last 54% are $q\bar{q}q\bar{q}$, ie. standard case 1 events.

Because the M1's and M2's in case 3 events of the $f\bar{f}$ background are very sensitive to the E_{cms}, the graphical cut has to be "pushed" up to higher M1's and M2's for higher energies. Since the M1 vs. M2 plots for the signals, and other backgrounds, doesn't vary much for the different energies, this "raising" of the cut reduces the efficiency for high energies.

The h^0A^0 and $f\bar{f}$ plots, with cuts, are shown for all energies in Fig. 6.13. All the available $f\bar{f}$ data are used. The h^0A^0 and $f\bar{f}$ on top of Fig. 6.13 are $E_{cms} = 175$ GeV, below are the plots for $E_{cms} = 192$ GeV, and at the bottom, $E_{cms} = 205$ GeV. The raising of the cut is clearly seen in this figure.

To make the plots in Fig. 6.13 more informative, the case 3 events from the $f\bar{f}$ background are extracted by two cuts. First, the $\chi^2_{tot} < 0.27E_{cms}$ cut to remove events with γ's down the beam pipe, and then the $N_{jets} > 3$ cut to assure extra jets. The plots show the h^0A^0 and $f\bar{f}$ events left after these two cuts. (In addition, the events are still required to have more than 9 tracks).

The graphical cut for $E_{cms} = 205$ GeV, in Fig. 6.13, might seem a bit too hard compared to 175, 192 GeV. This is however necessary because, in addition to the raising of M1 and M2 in $f\bar{f}$, more $f\bar{f}$ events survive the other cuts at $E_{cms} = 205$ GeV. The combination of the reduced efficiency of the other cuts, the bigger Z^0Z^0 cross section, and the raising of M1 and M2 for $f\bar{f}$, makes this hard graphical cut necessary for $E_{cms} = 205$ GeV.

The h^0,A^0 masses are (78,80) for 175 and 192, and (87,90) for $E_{cms} = 205$ GeV.

The resulting percentage of events left, after only this cut, is found in Table 6.7.

M1 vs. M2					
	h^0A^0	h^0Z^0	Z^0Z^0	$f\bar{f}$	W^+W^-
% left	90.6	64.1	48.7	9.4	50.5

Table 6.7: Percentage of events left after the graphical cut, for the data at $E_{cms} = 192$ GeV.

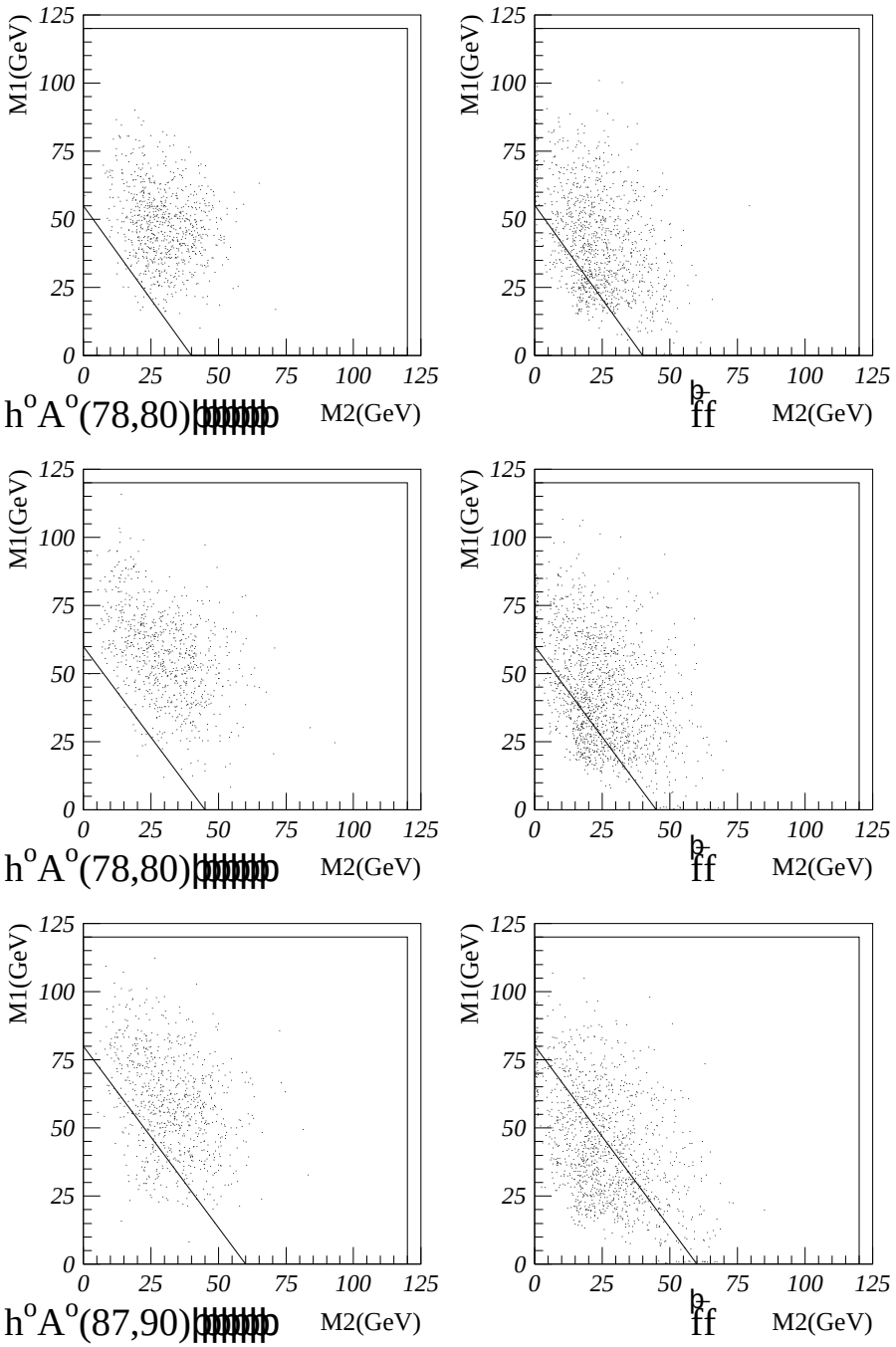

Figure 6.13: The graphical cut for different energies. The two plots on the top are for the E_{cms} = 175 GeV data. The two plots below are for the E_{cms} = 192 GeV data, and those at the bottom are for E_{cms} = 205 GeV.

6.2 Summary of Cuts

Values extracted after jet reconstruction to any number of jets:

Probp Positive N-track probability of the event (B-tag[21]).

$\boldsymbol{N_{jets}}$ Number of reconstructed jets (LUCLUS[20], $d_{join} = 5$ GeV).

$\boldsymbol{N^B_{jets}}$ Number of jets with probp< 0.05, #tracks≥ 3 and $E \geq 5$ GeV (JADE[20], $y_{join} = 0.01$).

$\boldsymbol{E_1}$ Energy of the jet with highest momentum (LUCLUS, $d_{join} = 5$ GeV).

Emcamax Biggest energy deposit in the EM calorimeters (FEMC or HPC).

Values extracted after forced 4-jet reconstruction (LUCLUS):

$\boldsymbol{\chi^2_{tot}}$ χ^2 of the energy, momentum conservation fit of the event (PUFIT[26]).

Values extracted after forced 2-jet reconstruction (LUCLUS):

M1 Invariant mass of the jet with highest momentum.

M2 Invariant mass of the other jet.

Cuts applied at		175 GeV	192 GeV	205 GeV
Probp	$<$	10^{-9}	10^{-9}	10^{-9}
N_{jets}	$>$	3	3	3
N^B_{jets}	$>$	2	2	2
E_1 (GeV)	$<$	61	75	86
Emcamax (GeV)	$<$	38	42	45
χ^2_{tot}	$<$	47	52	55
Plus graphical cut in M1 vs. M2				

Table 6.8: Summary of all the cuts at different energies.

Chapter 7

Results

After establishing the cuts, they must be put into action. This Chapter first presents the signal efficiencies, and then the backgrounds.

In addition to the background data presented in the previous Chapter, data at other nearby energies have been included. This is done to reduce the statistical errors.

All simulated data in this analysis are created by PYTHIA and JETSET, except for $(e^+e^-)f\bar{f}$ where the DELPHI generator TWOGAM[29] is used.

7.1 Signal Efficiencies

The signal efficiencies with statistical errors for all the available signal datasets are presented in Table 7.1. (The h^0 masses are calculated with $A = \mu = 0$). All the sets contain from 998 to 1000 events, except the last h^0Z^0 set ($E_{cms} = 205$ GeV), which only contains 193 events. The statistical errors are given by this formula:

$$\sigma_\epsilon = \frac{\sqrt{\epsilon(1-\epsilon)}}{\sqrt{N}}, \tag{7.1}$$

where N is the number of events in each dataset and ϵ is the efficiency of the cuts.

The h^0A^0 efficiencies are very good, while the h^0Z^0 efficiencies can be tripled by doing a $b\bar{b}q\bar{q}$ search instead of a $b\bar{b}b\bar{b}$ search, as mentioned in the previous Chapter.

7.2 Backgrounds

In this Section all the analysed backgrounds are presented. These include the three main energies and some nearby energies. New backgrounds are also presented. These can however hardly be called backgrounds, since none of their events pass the cuts.

The background data at the three main energies (175, 192 and 205 GeV) are all produced using the last version of DELSIM (V96), while the rest are generated with an older DELSIM version (V94). The biggest difference between them is in the Vertex Detector. The 96 VD is a little longer, and has end caps, making it better than the 94 configuration. This is mostly seen in the B-tagging, where the VD is vital.

7.2.1 Background Errors

Using simulated background data at nearby energies reduces the statistical errors significantly, but it also increases the systematical errors, since the data are generated with different DELSIM versions. The reduction of statistical errors is

Signal	m_{A^0} (GeV)	$\tan\beta$	m_{h^0} (GeV)	efficiency (%)
	175 GeV			
h^0A^0	70	3	61	28.2 ± 1.4
	70	10	69	28.7 ± 1.4
	80	3	67	26.5 ± 1.4
	80	10	78	32.3 ± 1.5
	85	3	70	31.2 ± 1.5
h^0Z^0			80	5.6 ± 0.7
			85	6.7 ± 0.8
	192 GeV			
h^0A^0	80	3	67	31.0 ± 1.5
	80	10	78	34.5 ± 1.5
	90	3	73	32.8 ± 1.5
	90	10	87	34.0 ± 1.5
	95	3	76	34.5 ± 1.5
h^0Z^0			80	6.2 ± 0.8
			85	6.2 ± 0.8
			90	6.5 ± 0.8
			95	6.3 ± 0.8
			100	6.3 ± 0.8
	205 GeV			
h^0A^0	90	3	73	29.0 ± 1.4
	90	10	87	32.1 ± 1.5
	95	3	76	30.2 ± 1.5
	95	10	92	30.0 ± 1.4
	100	3	78	30.8 ± 1.5
	105	2	70	30.3 ± 1.5
h^0Z^0			90	5.9 ± 0.7
			100	6.5 ± 0.8
			105	5.6 ± 0.7
			110	6.3 ± 1.8

Table 7.1: Signal efficiencies with statistical errors.

often bigger than the increased systematical errors, since the differences in energies and VD configurations are small compared to the big amount of additional simulated data obtained by including the 94 data. The 94 data are only included where the amount is big enough to make a significant improvement in statistical errors.

Since the systematical errors in this analysis are very hard to approximate, they've been omitted completely. The biggest problem concerning the systematical errors is the lack of real data, and the great amount of work needed to approximate them. Another complication is the improvements done on the detector every year, which also influences the systematical errors.

The statistical error for each of the backgrounds is:

$$\sigma_{bg} = k\sqrt{N_b(1 - \frac{N_b}{N_s})},$$

where k is the expected number of events for the given integrated Luminosity ($\int Ldt$ = 300, 500 pb^{-1}) divided by the number of simulated events, N_s. N_b is the number of events passing the cuts.

After calculating statistical errors for each background, they're all summed up to find the total statistical error, like this:

$$\sigma_{tot} = \sqrt{\sigma^2_{Z^0Z^0} + \sigma^2_{f\bar{f}} + \sigma^2_{W^+W^-}}$$

7.2.2 Applied Cuts

Presenting the efficiency for each cut separately, like in the previous Chapter, is quite interesting, but it's their combined efficiency that counts. The sequence of the cuts is very important for each cut's efficiency. Still, all cuts presented here remove some background, even when being last in the sequence. Tables 7.2 to 7.4 presents the background and signal events left after each cut, for each energy. The h^0 and A^0 masses are given, in GeV, in the parentheses. The numbers in each row are the events left after the cut presented in the same row, and the cuts follow the same sequence as in the previous Chapter. The first row is the available simulated events (# simulated), ie. no cut applied.

7.2.3 Total Backgrounds

The total backgrounds are presented in Tables 7.5 to 7.7. The efficiencies are the number of events passing the cuts divided by the total number of Simulated events. The integrated Monte Carlo (MC) luminosity is the integrated luminosity, $\int Ldt$, needed to produce the given number of simulated events.

When nearby energies are included, the total number of events, and the total number of events passing the cuts, are added into a total efficiency.

The W^+W^- errors at E_{cms} = 175 and 192 GeV are estimated by letting one event pass the cuts.

$E_{cms} = 175$ GeV							
Cut			h^0A^0 (78, 80)	h^0Z^0 (80)	Z^0Z^0	$f\bar{f}$	W^+W^-
#Simulated			1000	1000	1500	33860	5020
Probp	$<$	10^{-9}	480	164	53	583	4
N_{jets}	$>$	3	438	119	28	31	3
N^B_{jets}	$>$	2	353	60	8	3	1
E_1	$<$	61 GeV	335	60	6	3	0
Emcamax	$<$	38 GeV	335	60	6	2	0
χ^2_{tot}	$<$	47	327	59	6	1	0
M1 vs. M2			323	56	6	0	0

Table 7.2: The number of events left after each cut at $E_{cms} = 175$ GeV.

$E_{cms} = 192$ GeV							
Cut			h^0A^0 (78, 80)	h^0Z^0 (80)	Z^0Z^0	$f\bar{f}$	W^+W^-
#Simulated			1000	1000	8650	39860	10910
Probp	$<$	10^{-9}	497	192	432	735	1
N_{jets}	$>$	3	449	136	301	52	1
N^B_{jets}	$>$	2	357	74	124	7	0
E_1	$<$	75 GeV	352	71	122	5	0
Emcamax	$<$	42 GeV	352	71	119	5	0
χ^2_{tot}	$<$	52	348	64	117	1	0
M1 vs. M2			345	62	113	1	0

Table 7.3: The number of events left after each cut at $E_{cms} = 192$ GeV.

$E_{cms} = 205$ GeV							
Cut			h^0A^0 (87, 90)	h^0Z^0 (90)	Z^0Z^0	ff	W^+W^-
#Simulated			998	1000	1000	36650	5000
Probp	$<$	10^{-9}	492	198	44	603	3
N_{jets}	$>$	3	461	145	32	37	1
N^B_{jets}	$>$	2	369	72	12	6	1
E_1	$<$	86 GeV	367	72	12	5	1
Emcamax	$<$	45 GeV	366	72	12	4	1
χ^2_{tot}	$<$	55	355	65	11	4	1
M1 vs. M2			321	59	10	2	1

Table 7.4: The number of events left after each cut at $E_{cms} = 205$ GeV.

Background	σ (pb)	E_{cms} (GeV)	Efficiency	MC $\int Ldt$ (pb^{-1})	Expected events $\int Ldt = 500$ pb^{-1}
Z^0Z^0	0.46	175	6/1500	3260	0.9 ± 0.4
ff	175	170	0/26940		
		175	0/33860		
		180	1/22280		
			1/83080	470	1.1 ± 1.1
W^+W^-	15	170	0/1070		
		175	0/5020		
		180	0/17020		
			0/23110	1540	$0 + 0.3$
$We\nu$	0.65	170	0/1000		
		175	0/2750		
		180	0/1000		
			0/4750	7310	0
$Z^0e^+e^-$	6.7	170	0/1000		
		175	0/2700		
		180	0/1000		
			0/4700	700	0
Total background					2.0 ± 1.2

Table 7.5: The total background at $E_{cms} = 175$ GeV.

Background	σ (pb)	E_{cms} (GeV)	Efficiency	MC $\int Ldt$ (pb^{-1})	Expected events $\int Ldt = 300\ \mathrm{pb}^{-1}$
Z^0Z^0	1.22	192	113/8650	7090	4.8 ± 0.4
ff	134	190	1/63260		
		192	1/39860		
			2/103120	770	0.8 ± 0.6
W^+W^-	18	190	0/11210		
		192	0/10910		
			0/22120	1230	$0 + 0.2$
Weν	0.83	190	0/1000		
		192	0/1000		
			0/2000	2410	0
$Z^0e^+e^-$	6.7	190	0/1980		
		192	0/3220		
			0/5200	780	0
$(e^+e^-)ff$	25	190	0/5900		
		192	0/11250		
			0/17150	690	0
Total background					5.6 ± 0.7

Table 7.6: The total background at $E_{cms} = 192$ GeV.

Background	σ (pb)	E_{cms} (GeV)	Efficiency	MC $\int Ldt$ (pb^{-1})	Expected events $\int Ldt = 300\ \mathrm{pb}^{-1}$
Z^0Z^0	1.47	205	10/1000	680	4.4 ± 1.4
ff	111	200	1/18450		
		205	2/36650		
		210	1/14550		
			4/69650	630	1.9 ± 1.0
W^+W^-	18	200	0/2110		
		205	1/5000		
		210	0/2400		
			1/9510	530	0.6 ± 0.6
Weν	1.0	200	0/1000	1000	0
$Z^0e^+e^-$	7.3	200	0/970		
		205	0/1490		
		210	0/990		
			0/3450	470	0
Total background					6.9 ± 1.8

Table 7.7: The total background at $E_{cms} = 205$ GeV.

7.3 Exclusion and Discovery Limits

After having found the signal efficiencies and backgrounds, the exclusion and discovery limits must be determined. Since the minimal supersymmetric Higgs sector has 2 free variables (at the tree level), m_{A^0} and $tan\beta$, the limits must be presented in 2 dimensional plots.

The limits are calculated from the backgrounds, their errors, and the expected $\int Ldt$. They are calculated with the prescription agreed on by all the LEP experiments[30] (exclusion= 95% CL, discovery$\approx 5\sqrt{bg}$). The limits are presented in Table 7.8. The number of observed events has to be below, or equal to, the exclusion limit for an exclusion, and above, or equal to, the discovery limit for a discovery. This means that if the number of observed events at $E_{cms} = 175$ GeV is 10, it'll be too high to exclude a signal and too low to be sure of a signal. If 7 events are observed, they can be excluded as background, and if 15 are observed it's time to open the Champagne bottles.

To put it short; When the number of observed events passes the exclusion limit, it can no longer be treated as a fluctuation of the background, and when it reaches the discovery limit, a signal is surely seen.

The observed numbers of events are integers, and since the calculated limits aren't, rounding has to be done. If an exclusion limit of 13.5 is calculated this means that 13 observed events is an exclusion and 14 isn't. The exclusion limits must therefore be rounded down. If on the other hand a discovery limit of 13.5 is calculated, this means that 14 observed events is a discovery and 13 isn't. The discovery limit must therefore be rounded up. All the limits in Table 7.8 have been rounded in this manner.

The number of observed events is the signal plus the background. The backgrounds are considered known, and the signal is given by:

$$\text{Signal} = \epsilon_{h^0A^0} * \sigma_{h^0A^0} * \int Ldt + \epsilon_{h^0Z^0} * \sigma_{h^0Z^0} * \int Ldt$$

Since the h^0A^0 and h^0Z^0 efficiencies for the different mass combinations of m_{h^0} and m_{A^0} are quite similar, average efficiencies can be used for each energy. This opens the chance to exclude or discover many m_{A^0}, m_{h^0} combinations with only one set of cuts.

The average efficiencies, $\epsilon_{h^0A^0}$ and $\epsilon_{h^0Z^0}$, with statistical errors, are given in Table 7.8. They are calculated by adding all the datasets, found in Table 7.1, for each signal at each energy, and by using Eq. (7.1).

7.3.1 Exclusion and Discovery Plots

Figs. 7.1 to 7.6 show the exclusion and discovery contours in the distributions of the observed (signal+background) number of events. These distributions depend

E_{cms} (GeV)	$\int Ldt$ (pb^{-1})	Background	Exclusion (Observed)	Discovery (Observed)	$\epsilon_{h^0A^0}$ (%)	$\epsilon_{h^0Z^0}$ (%)
175	500	2.0 ± 1.2	7	15	29.4 ± 0.6	6.2 ± 0.5
192	300	5.6 ± 0.7	12	22	33.4 ± 0.7	6.3 ± 0.3
205	300	6.9 ± 1.8	14	25	30.4 ± 0.6	6.0 ± 0.4

Table 7.8: The exclusion, discovery limits, and average efficiencies with statistical errors for h^0A^0 and h^0Z^0.

only upon m_{A^0} and $\tan\beta$ on the tree level, but many other parameters are introduced in the loop corrections. As mentioned earlier, it was agreed to plot the exclusion and discovery contours with m_{A^0} between 0 and 400 GeV, and $\tan\beta$ between 1 and 60. The contours just become straight lines when going above these limits.

Since many unknown parameters appear in the loop corrections (this analysis includes 1 and 2 loop corrections), three different combinations of the most important correction parameters are plotted. M_S is kept at 1 TeV, while A and μ are varied between extremities.

Since the backgrounds are constant over the m_{A^0}-$\tan\beta$ plane, the only variation in the plots comes from the signal. And, since the efficiencies and integrated luminosities also are constant over the m_{A^0}-$\tan\beta$ plane, the variation in the plots arise solely from variations in the h^0A^0 and h^0Z^0 cross sections. As seen in Fig. 3.3, $\sigma_{h^0A^0}$ is biggest for small m_{A^0} values and $\sigma_{h^0Z^0}$ is biggest for small $\tan\beta$ values. The distribution of the observed events is similar to the sum of $\sigma_{h^0A^0}$ and $\sigma_{h^0Z^0}$, with the latter being suppressed by a factor of 5 due to lower efficiency.

In the exclusion plots, the filled areas (m_{A^0}, $\tan\beta$ combinations) to the left of, and below the contours, produce enough signal to push the observed number of events above the exclusion limit. If the limit isn't passed, no signal is seen and these regions can be excluded.

In the discovery plots, the filled areas (m_{A^0}, $\tan\beta$ combinations) to the left of, and below the contours, produce enough signal to push the observed number of events above the discovery limit. A discovery is therefore possible in these regions.

When examining these plots closer one might be surprised that while the excluded regions of the exclusion plots increase with higher energies, the regions in the discovery plots decrease. This happens for several reasons; First, the cross sections of h^0A^0 and h^0Z^0 cover greater areas in the m_{A^0}-$\tan\beta$ plane at higher energies (192, 205 GeV), but their values in the low m_{A^0}-$\tan\beta$ regions decrease when compared to 175 GeV. Second, the discovery limits for 192 and 205 GeV are considerably higher than that of 175 GeV. Third, the integrated luminosity

at 192, 205 GeV is smaller than that of 175 GeV.

The consequence is that the exclusion limits for 192 and 205 GeV are low enough to benefit from the increased cross sections at higher m_{A^0} and $\tan\beta$, while the discovery limits are too high to benefit from this increase. Instead the discovery regions suffer from lower integrated luminosity, and lower cross sections in the low m_{A^0}-$\tan\beta$ region, at 192 and 205 GeV.

To make the exclusion limit for the h^0 mass clearer, a m_{A^0}-m_{h^0} plot is included, Fig. 7.7. This includes the excluded region at each energy and the unphysical region for the h^0 mass. The excluded regions are calculated with $A = \mu = 0$ and the unphysical region is above the h^0 mass calculated with $\tan\beta = 60$ and $A = \sqrt{6}M_S, \mu = 0$.

Similar plots for other A and μ combinations, and for the discovery limits, aren't included because within these plots h^0 can't be excluded or discovered in the high-m_{A^0} region. No exclusion or discovery limit on m_{h^0} can therefore be obtained, for the whole $m_{A^0} \in \{0, 400 \text{ GeV}\}$ region, from these plots, except from the trivial $m_{h^0} > 0$ limit.

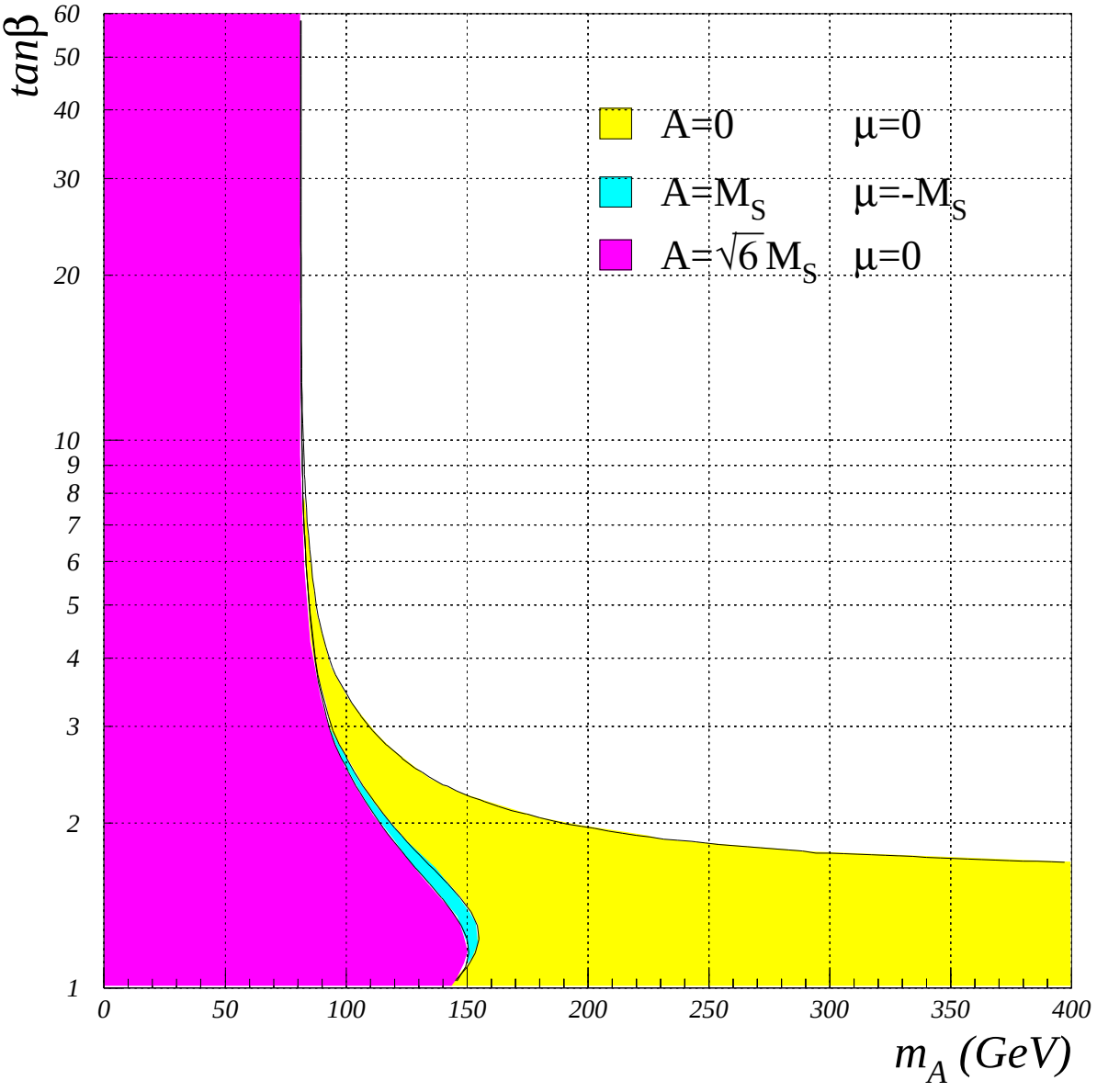

Figure 7.1: The exclusion plot for $E_{cms} = 175$ GeV. The integrated Luminosity is 500 pb^{-1}, and $M_S = 1$ TeV.

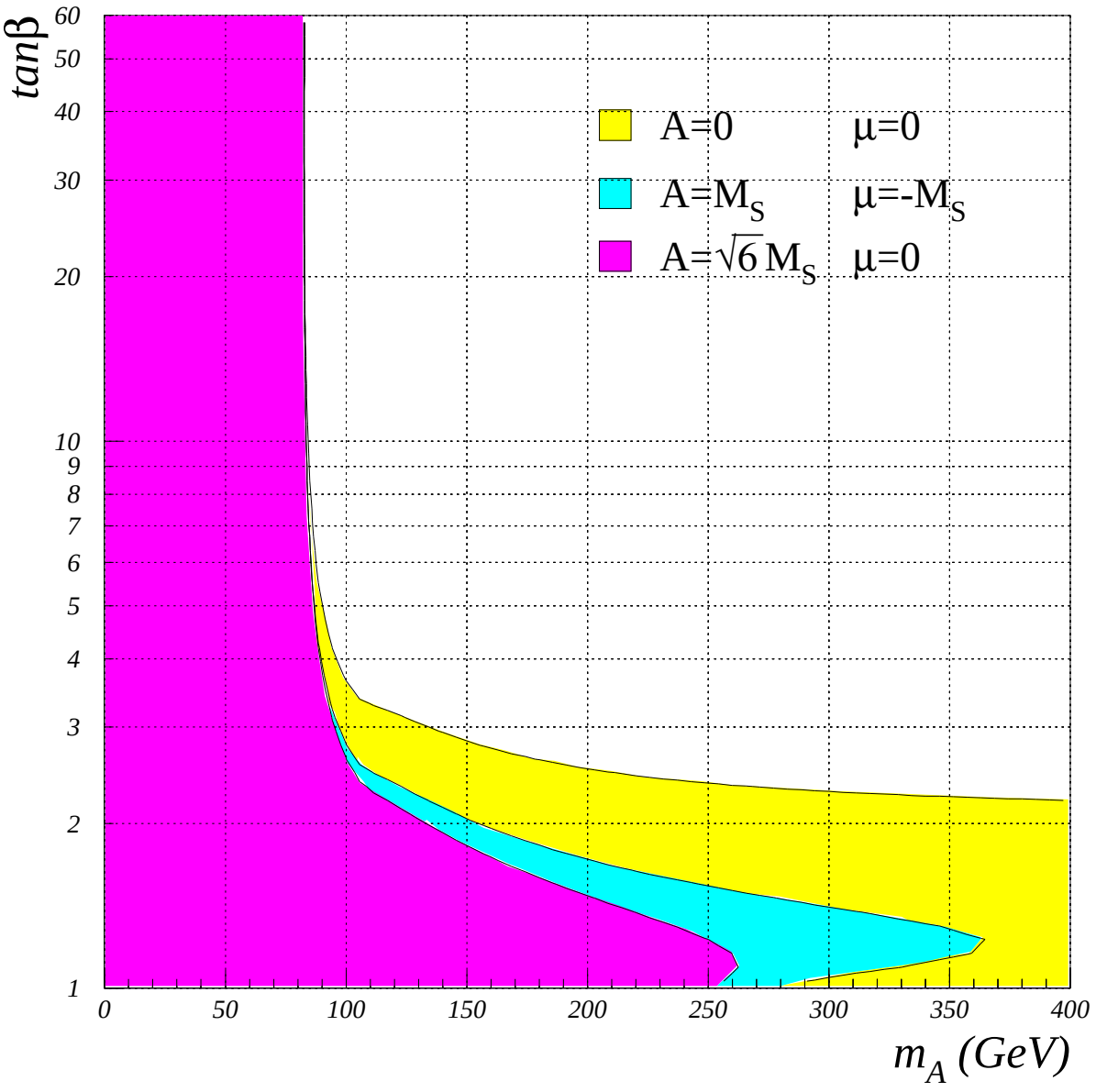

Figure 7.2: The exclusion plot for $E_{cms} = 192$ GeV. The integrated Luminosity is 300 pb^{-1}, and $M_S = 1$ TeV.

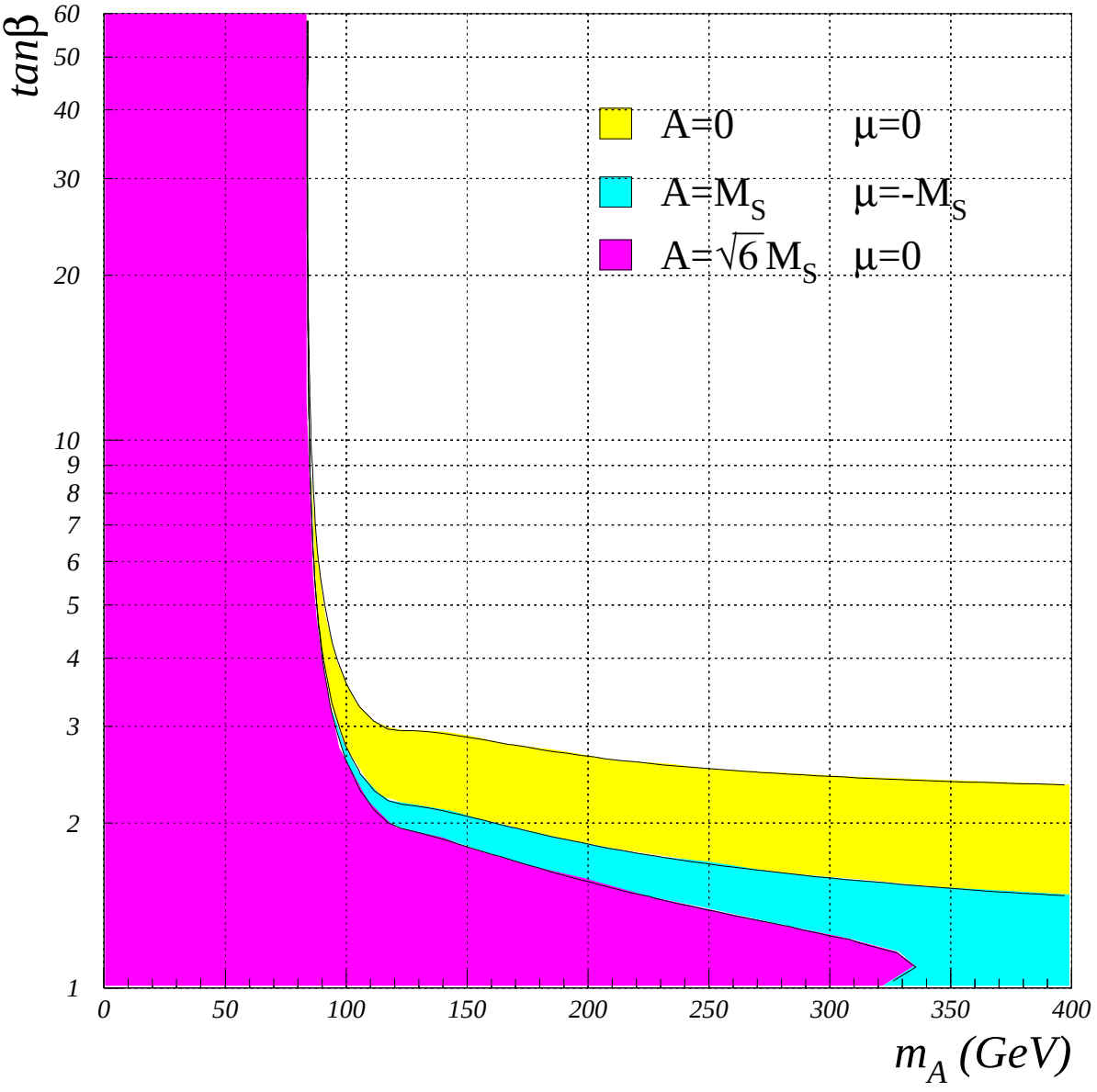

Figure 7.3: The exclusion plot for $E_{cms} = 205$ GeV. The integrated Luminosity is 300 pb^{-1}, and $M_S = 1$ TeV.

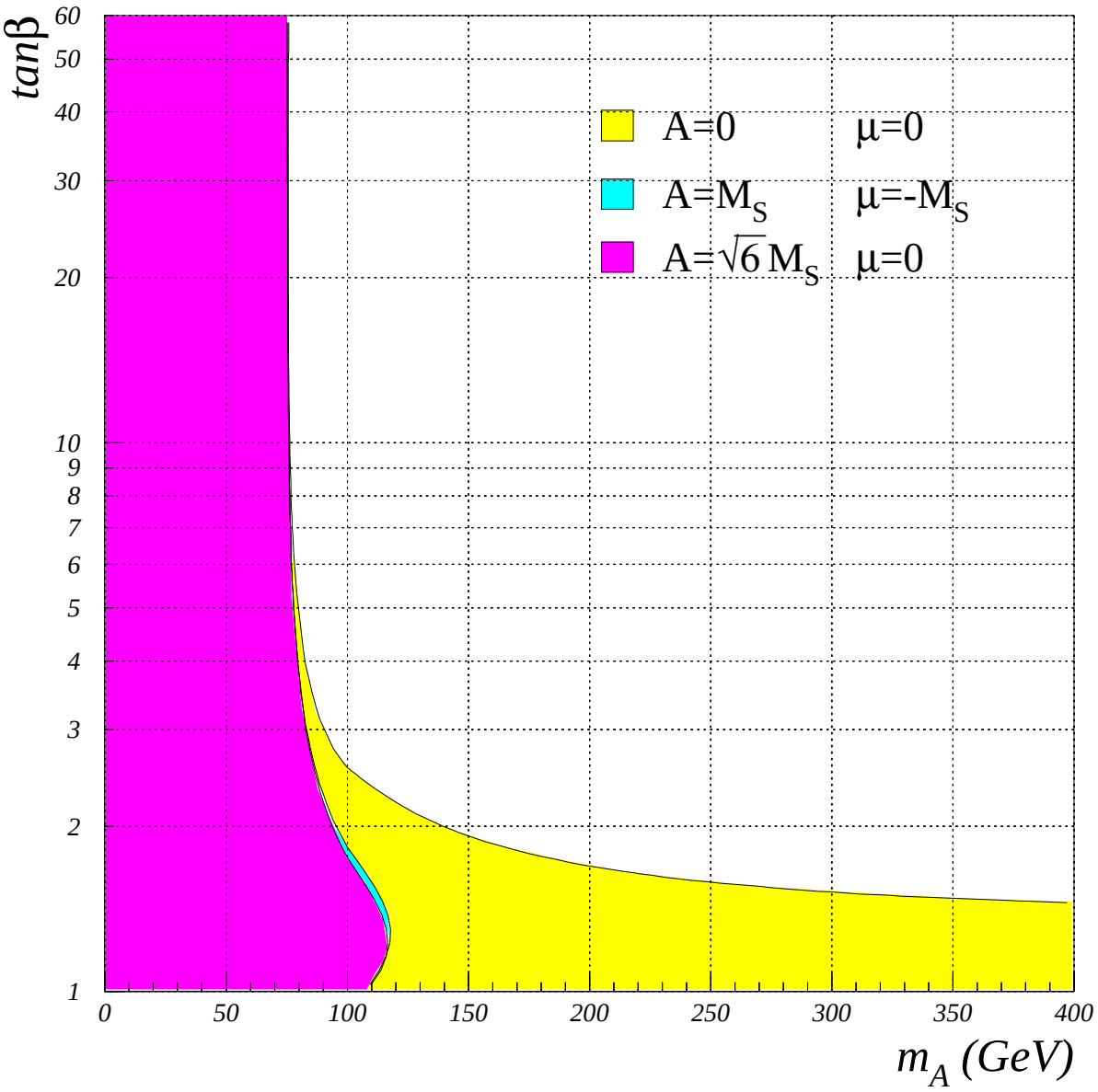

Figure 7.4: The discovery plot for $E_{cms} = 175$ GeV. The integrated Luminosity is 500 pb^{-1}, and $M_S = 1$ TeV.

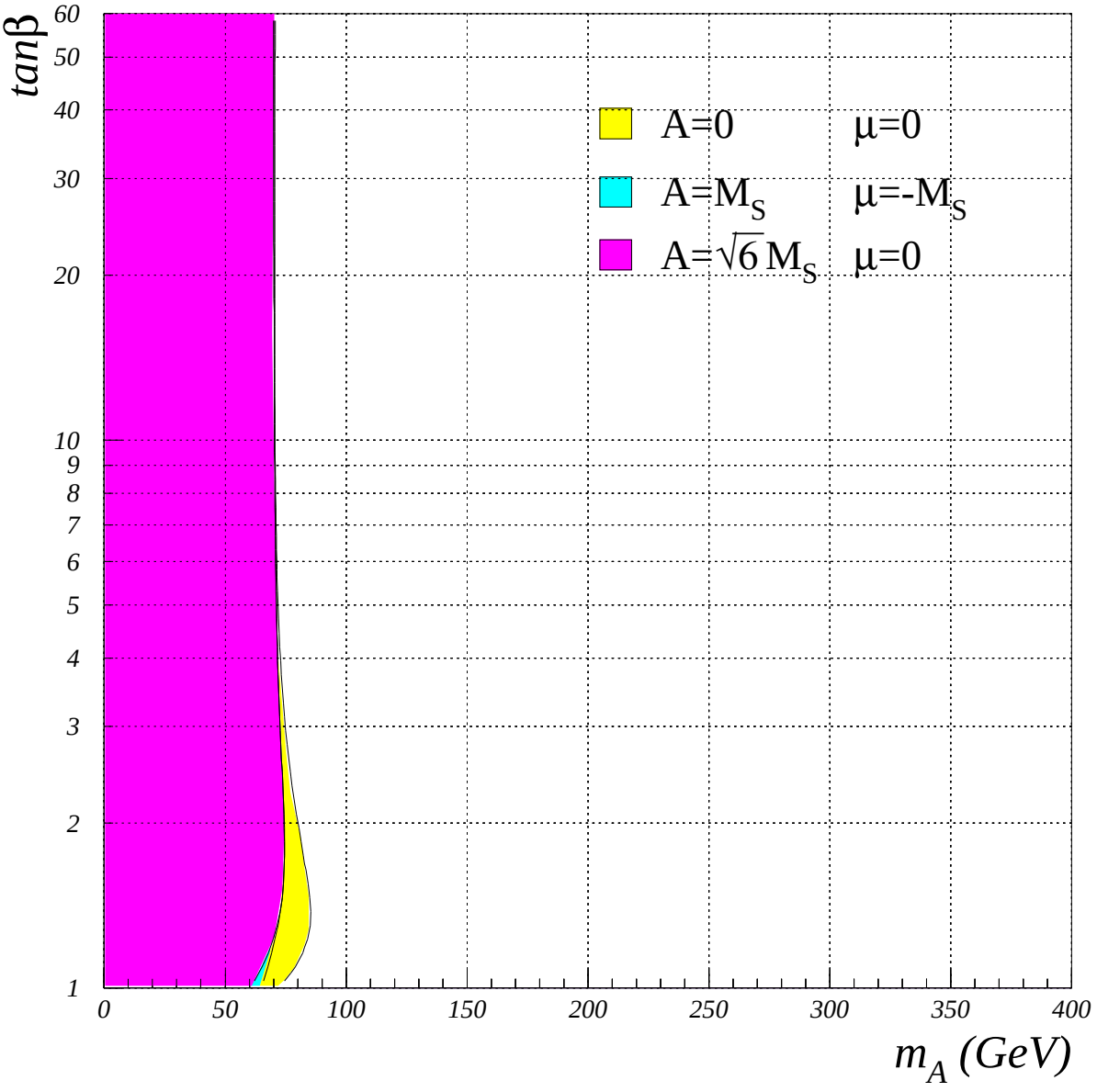

Figure 7.5: The discovery plot for E_{cms} = 192 GeV. The integrated Luminosity is 300 pb^{-1}, and M_S = 1 TeV.

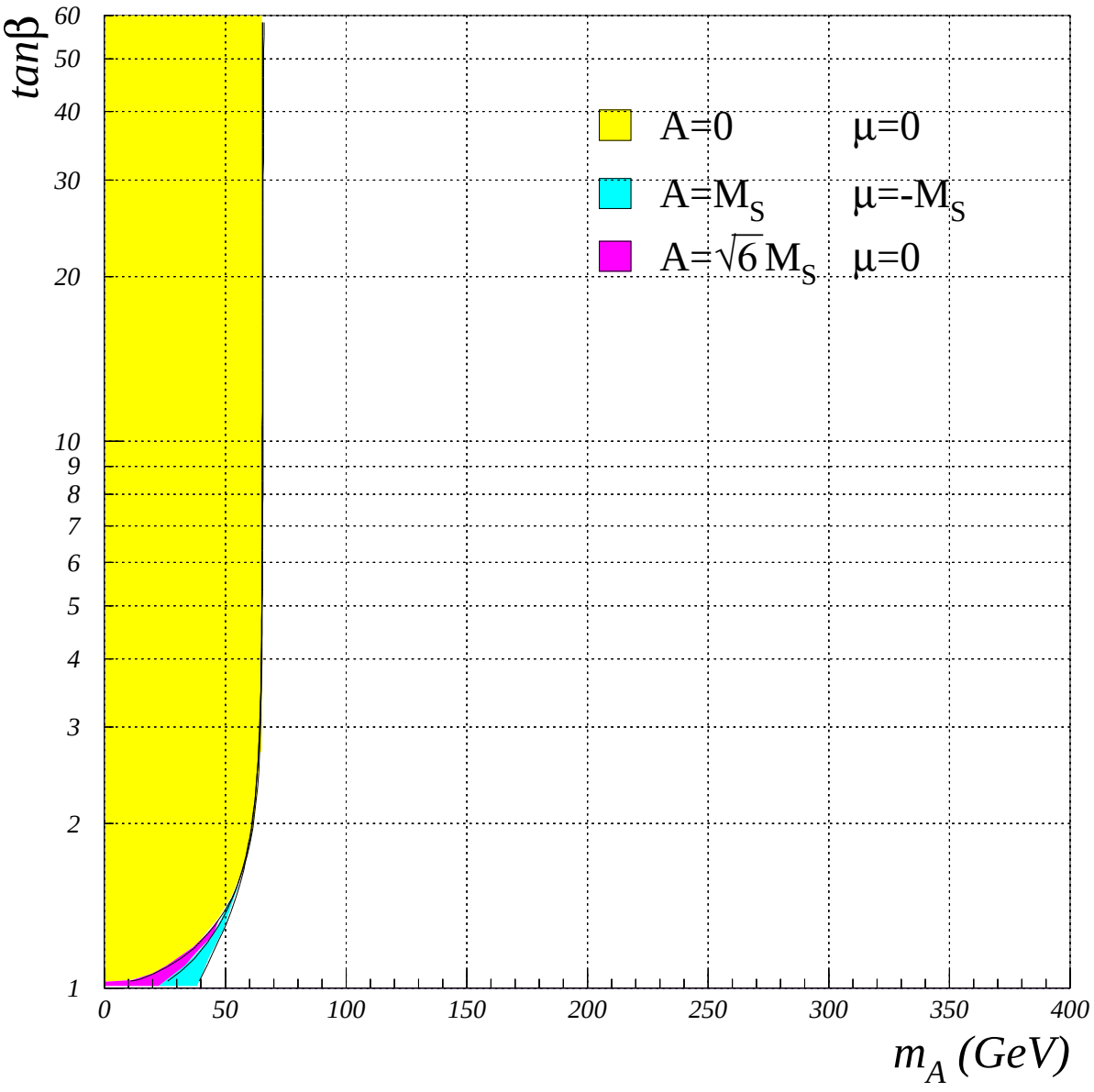

Figure 7.6: The discovery plot for $E_{cms} = 205$ GeV. The integrated Luminosity is 300 pb^{-1}, and $M_S = 1$ TeV.

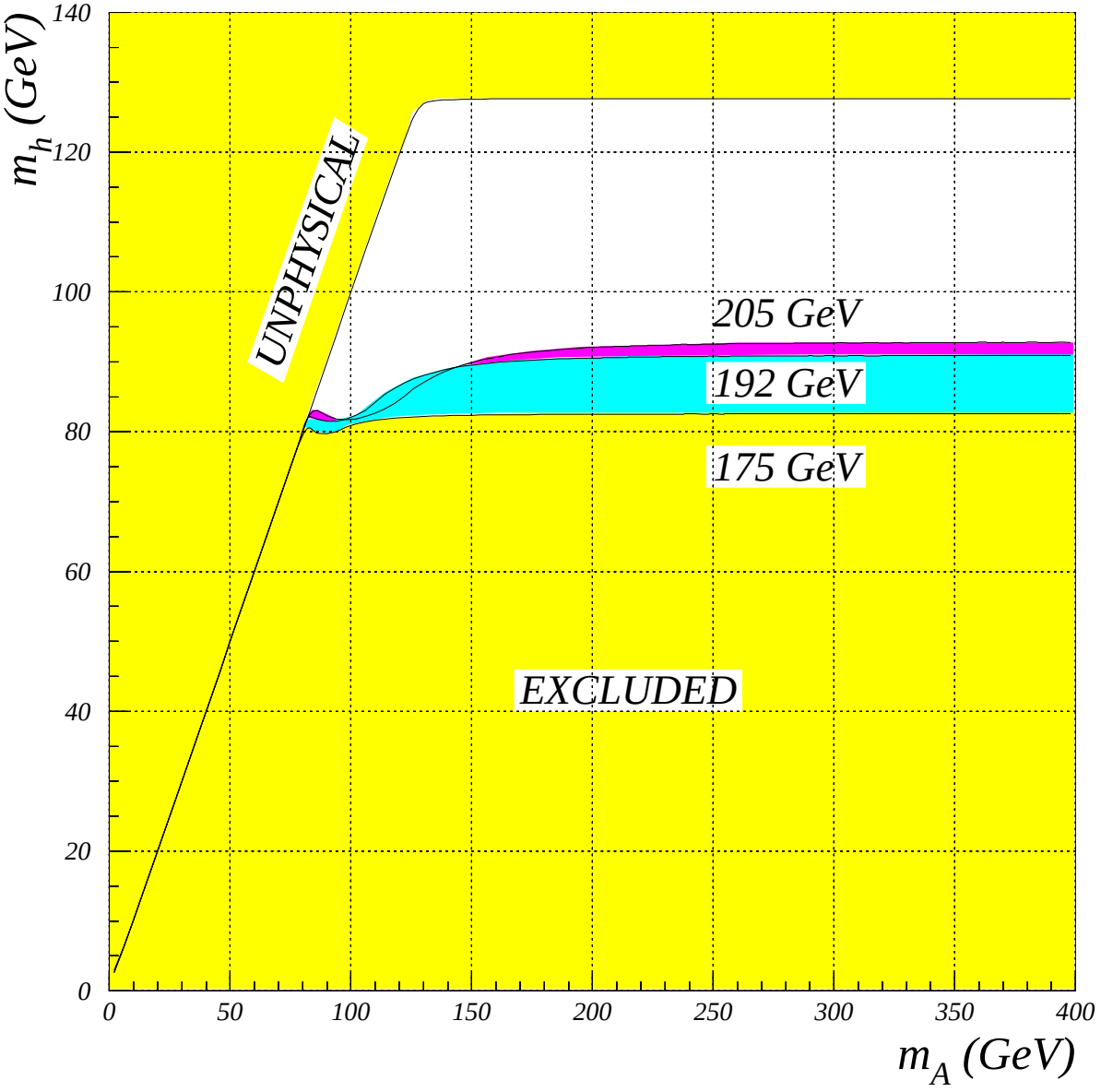

Figure 7.7: The exclusion plot for $A = \mu = 0$, and $M_S = 1$ TeV. The integrated Luminosity for $E_{cms} = 175$ GeV is 500 pb^{-1}, and 300 pb^{-1} for the other energies. The unphysical region is above the h^0 mass calculated with $\tan\beta = 60$ and $A = \sqrt{6}M_S, \mu = 0$.

Chapter 8

Conclusion

As mentioned in the beginning of this thesis, the h^0 is excluded (95% CL) up to a mass of 44 GeV (without radiative corrections, ie. $A = \mu = 0$), and A^0 is excluded up to a mass of 22 GeV[3].

8.1 Final m_{A^0} and m_{h^0} Limits at LEP2

The m_{A^0} exclusion limits obtained, for all A, μ combinations, from full LEP2 simulations, are:

- 82 GeV at $E_{cms} = 175$ GeV. (Kinematical limit = 87 GeV).
- 83 GeV at $E_{cms} = 192$ GeV. (Kinematical limit = 96 GeV).
- 85 GeV at $E_{cms} = 205$ GeV. (Kinematical limit = 102 GeV).

The m_{A^0} discovery limits obtained, for all A, μ combinations, from full LEP2 simulations, are:

- 75 GeV at $E_{cms} = 175$ GeV.
- 70 GeV for $\tan\beta \geq 1.3$, and 60 GeV for $\tan\beta < 1.3$, at $E_{cms} = 192$ GeV.
- 65 GeV for $\tan\beta \geq 4$, and 0 GeV for $\tan\beta < 4$, at $E_{cms} = 205$ GeV.

The m_{h^0} exclusion limits obtained for $A = \mu = 0$, from full LEP2 simulations, are:

- 79 GeV at $E_{cms} = 175$ GeV.
- 82 GeV at $E_{cms} = 192$ GeV.
- 82 GeV at $E_{cms} = 205$ GeV.

For the other A, μ combinations, and for the discovery plots, no m_{h^0} limit can be set in the whole $m_{A^0} \in \{0, 400 \text{ GeV}\}$ region.

The m_{A^0} limits are strongly dictated by $\sigma_{h^0 A^0}$ which falls to zero before m_{A^0} reaches $\frac{1}{2}E_{cms}$, in the $\tan\beta > 10$ region. This happens because $m_{A^0} \approx m_{h^0}$ and $\sigma_{h^0 Z^0} \approx 0$ in this high-$\tan\beta$ region.

For $\tan\beta < 10$ the h^0A^0 cross section drops at an even quicker rate, Fig. 3.3. This region is however covered by h^0Z^0.

So, while the m_{h^0} limits can be raised even further through a dedicated h^0Z^0 search ($b\bar{b}q\bar{q}$), the m_{A^0} limits can only be raised significantly by going to higher energies.

Since $\sigma_{h^0 A^0}$ drops much quicker when going to higher m_{A^0} than $\sigma_{h^0 Z^0}$ does when going to higher $\tan\beta$, increased $\int Ldt$ expands the low-$\tan\beta$ regions much more than the high-$\tan\beta$ regions in the exclusion and discovery plots, Figs. 7.1 to

7.6. Even with a huge rise in $\int Ldt$, the "hole" just right of the kinematical limit for $\sigma_{h^0A^0}$, at high $\tan\beta$, isn't excluded. The same is seen when combining data from the 4 different experiments, which is, in effect, the same as quadrupling the $\int Ldt$.

If gauge, Yukawa coupling unification, and spontaneous electroweak symmetry breaking[2, 31] are required simultaneously, the Minimal Supersymmetric Model is reduced to the Constrained Minimal Supersymmetric Model. This theory has a more restricted parameter space than the Minimal Supersymmetric Model, and it favors a $\tan\beta$ value of 1.5 or 47. As seen in the exclusion plots, the lower value of $\tan\beta$ can be excluded for $A = \mu = 0$ at all energies.

In the Minimal Supersymmetric Model the upper limit for m_{h^0} is around 130 GeV. Currently favored grand unified models however prefer a h^0 mass below 100 GeV[31], which might be accessible at LEP2 with $E_{cms} = 192$ GeV, a high $\int Ldt$ and the combined results of the 4 experiments.

The Standard Model Higgs mass limit is improved from 65 GeV[4] to around $E_{cms} - 100$ GeV, at LEP2[2].

If no signs of Higgs bosons are seen at LEP2, the next chance to find them is at LHC. The $E_{cms} = 14$ TeV at LHC is enough for the discovery or final death of the Higgs bosons.

8.2 Possible Improvements to the Analysis

The classification of B-jets is very simple in this thesis, and can probably be improved by looking at jet-charge and the particle content of the jets. In addition, the B-tagging program[21] version used in this thesis doesn't look at the z information from the Vertex Detector. This is included in newer versions of the B-tagging and should increase efficiency a little.

Bibliography

[1] P.W. Higgs, *Phys. Lett.* **12** (1964) 132, *Phys. Rev. Lett.* **13** (1964) 508, *Phys. Rev.* **145** (1966) 1156; F. Englert and R. Brout, *Phys. Rev. Lett* **13** (1964) 321; G.S. Guralnik, C.R Hagen and T.W.B. Kibble, *Phys. Rev. Lett* **13** (1964) 585; T.W.B. Kibble, *Phys. Rev.* **155** (1967) 1554.

[2] DELPHI Collaboration, *Higgs boson search at LEP200 with DELPHI.* DELPHI 95-57 PHYS 493, 12 July 1995.

[3] Particle Data Group, *Review of Particle Properties*, Physical Review **D50**, (1994) 1173

[4] Jorge L. Lopez, *SuperSymmetry: From the Fermi Scale to the Planck Scale.* DOE/ER/40717-23, hep-ph/9601208. To appear in Reports on Progress in Physics.

[5] J.F. Gunion, H.E. Haber, G. Kane and S. Dawson, *The Higgs Hunter's Guide.* Frontiers in Physics Series (Vol. 80), ISBN 0-201-50935-0. 1990.

[6] DELPHI Collaboration, *Nuclear Instruments and Methods in Physics Research* **A303** (1991) 233-276.

[7] Howard E. Haber and G.L. Kane, *Phys. Rep.* **117**(1985) 75.

[8] C.H. Llewellyn Smith and G.G. Ross, *Phys. Lett.* **105B** (1981) 38.

[9] André Sopczak, *Search for Non-Minimal Higgs Bosons in Z^0 Decays with the L3 Detector at LEP.* Ph.D dissertation submitted October 1992 to the University of California, San Diego.

[10] Gordon L. Kane and Howard E. Haber, *Perspectives on Higgs Physics.* Advanced Series on Directions in High Energy Physics–Vol.13. ISBN 981-02-1216-X. 1993.

[11] M. Carena, J.R. Espinosa, M. Quiros and C.E.M. Wagner, CERN preprint CERN-TH/95-45.

[12] H.P. Nilles, *Phys. Rep.* **110**(1984) 1.

[13] S. Pokorski, in *New Theories in Physics, Proceedings of the XI Warzaw Symposium on Elementary Particle Physics,* Kazimierz, Poland, 1988. Edited by Z. Ajduk, S. Pokorski and A. Trautman (World Scientific, Singapore, 1989) p. 36.

[14] J. Bjorken, *Proceedings of the 1976 SLAC summer Institute on Particle Physics*, ed. by M.C. Zipf (SLAC Report 198, 1977) p. 1.

[15] G. Pocsik and G. Zsigmond, *Z. Phys.* **C10**(1981) 367.

[16] ISR corrections provided by Celso Martinez from Santander University, Spain.

[17] J. Ellis, G. Ridolfi and F. Zwirner, *Phys. Lett.* **B257** (1991) 83; *Phys. Lett.* **B262** (1991) 477.

[18] Made by Vidar Lund at Oslo University, Norway.

[19] H.-U. Bengtsson and T. Sjöstrand, Computer Physics Commun. **46** (1987) 43.

[20] T. Sjöstrand, Computer Physics Commun. **39** (1986) 347; T. Sjöstrand and M. Bengtsson, Computer Physics Commun. **43** (1987) 367.

[21] D. Brown and M. Frank, *Tagging b hadrons using track impact parameter*, ALEPH 92-135, PHYSIC 92-124; G.V. Borisov, *Lifetime Tag of events* $Z^0 \to b\bar{b}$ *with the DELPHI detector. AABTAG program.* DELPHI 94-125 PROG 208, 11 August 1994.

[22] DELPHI collaboration, DELPHI 89-44 PROG 137, 17 May 1989.

[23] DELPHI Collaboration, DELPHI 94-161 PROG 210, 20 December 1994.

[24] DELPHI Collaboration, DELPHI 92-118 PROG 189, 5 September 1994.

[25] DELPHI Collaboration, DELPHI 89-67 PROG 142, 10 July 1989.

[26] N. Kjær and R. Møller *Reconstruction of Invariant Masses in Multi-Jet Events*, DELPHI 91-17 PHYS 88, 25 April 1991.

[27] S. Bethke, Z. Kunszt, D.E. Soper and W.J. Stirling, *Nucl. Phys.* **B370**(1992)310.

[28] DELPHI Collaboration, DELPHI 92-166 PHYS 250, 17 December 1992.

[29] S. Nova et al. *MONTE-CARLO Event Generator for two Photon Physics.* DELPHI 90-35 PROG 152, 19 November 1990.

[30] Appendix, Interim report on the physics motivations for an energy upgrade of LEP2, by the Workshop on Physics at LEP2, CERN-TH/95-151, CERN-PPE/95-78.

[31] V. Barger et al., *Phys. Lett.* **B314** (1993) 351, *Phys. Rev.* **D49** (1994) 4908; G.L. Kane et al., *Phys. Rev.* **D49** (1994) 6173; W. de Boer, R. Ehret, D.I. Kazakov, *Phys. Lett.* **B334** (1994) 220, *Z. Phys.* to be published; M. Carena and C.E.M. Wagner, CERN preprint CERN-TH/7393, July 1994.